Journal of Computational Physics 313 (2016) 121–143

Contents lists available at ScienceDirect

Journal of Computational Physics

www.elsevier.com/locate/jcp

A Cartesian scheme for compressible multimaterial models in 3D

Alexia de Brauer [a,b,c], Angelo Iollo [a,b,c,*], Thomas Milcent [d,e]

[a] Univ. Bordeaux, IMB, UMR 5251, F-33400 Talence, France
[b] CNRS, IMB, UMR 5251, F-33400 Talence, France
[c] INRIA, F-33400 Talence, France
[d] Univ. Bordeaux, I2M, UMR 5295, F-33400 Talence, France
[e] Arts et Métiers Paristech, F-33607 Pessac, France

ARTICLE INFO

Article history:
Received 11 April 2015
Received in revised form 6 February 2016
Accepted 11 February 2016
Available online 17 February 2016

Keywords:
Compressible multimaterial
Immersed boundary
Eulerian elasticity

ABSTRACT

We model the three-dimensional interaction of compressible materials separated by sharp interfaces. We simulate fluid and hyperelastic solid flows in a fully Eulerian framework. The scheme is the same for all materials and can handle large deformations and frictionless contacts. Necessary conditions for hyperbolicity of the hyperelastic neohookean model in three dimensions are proved thanks to an explicit computation of the characteristic speeds. We present stiff multimaterial interactions including air–helium and water–air shock interactions, projectile-shield impacts in air and rebounds.

© 2016 Elsevier Inc. All rights reserved.

1. Introduction

The study of three-dimensional multimaterial phenomena requires efficient numerical modeling and simulation. These problems are insoluble by traditional theoretical and experimental approaches and hazardous to study in the laboratory. Nevertheless, their accurate and efficient simulation is crucial to reduce environmental impact in many industrial domains. Numerical model research in this field is particularly active because of the formidable difficulty in applying classical approaches based on *ad hoc* models and schemes to multi-physics contexts.

In what follows we focus on phenomena that involve gases, liquids and elastic materials undergoing rapid evolution and large deformations in three space dimensions. For this reason, we privilege a fully Eulerian approach and a monolithic model that describes each material by the same set of conservation equations and an appropriate thermodynamically consistent constitutive law different for each material [15]. For specific applications, typically in presence of mostly radial phenomena, Lagrangian or Lagrangian–Eulerian approaches may be more pertinent, see [20,13,6,21].

Fully Eulerian hyperbolic conservative models for continuum mechanics were introduced in [15,26,27] and their numerical analysis started in [12,24]. In [12] the authors propose a scheme, the ghost-fluid method, that allows an implicit capturing of the material interfaces. Moreover, they devise a locally non-conservative Godunov solver at the interface that is stable and non-oscillatory. This scheme relies on the definition of a ghost medium that requires the storage of additional variables at the material interfaces, where the solution of two Riemann problems, each relative to a different material, is necessary. A different method was proposed in [24] where a conservative cut-cell technique was developed for hyperelastic

* Corresponding author at: Univ. Bordeaux, IMB, UMR 5251, F-33400 Talence, France.
E-mail addresses: alexia.de-brauer@math.u-bordeaux1.fr (A. de Brauer), angelo.iollo@math.u-bordeaux1.fr (A. Iollo), thomas.milcent@u-bordeaux.fr (T. Milcent).

http://dx.doi.org/10.1016/j.jcp.2016.02.032
0021-9991/© 2016 Elsevier Inc. All rights reserved.

and plastic multimaterial simulations. A specific feature of this numerical model is that the deviations of the deformation gradient with respect to the irrotational compatibility condition and to continuity equation are explicitly penalized in the governing equations. This scheme is at the base of many other subsequent works in the literature.

Another approach is introduced in [11] for hyperelastic solid and fluid interactions. The authors design a conservative non-equilibrium mixture model that relaxes to the desired multimaterial conservation laws. In this approach one compromises on the sharpness of the material interface to avoid oscillations and to apply an HLLC solver previously developed for a single material in [14]. Further developments of this method include plasticity modeling [10] and an hyperbolic sub-system splitting procedure [9] where each sub-system has only three waves instead of seven.

The analysis and the simulation of three-dimensional hyperelastic models present specific difficulties due to the seven-wave pattern and to the inherent hyperbolicity constraint. In [4] an approximation of the Riemann problem based on characteristic tracing is employed to simulate the one-dimensional projection of the seven-wave pattern typical of a three-dimensional hyperelastic constitutive law. This approach has further been developed in [3] to deal with actual multimaterial interfaces thanks to a variant of the ghost-fluid method, with applications to one-dimensional as well as two-dimensional deformations of multiple hyperelastic sliding materials. A fully conservative cut-cell three-dimensional Eulerian method is then presented in [5] for simulating multiple compressible solid and fluid components where internal boundaries are tracked using level set functions. A different discretization scheme is adopted in [17], where the simulation of elastic and plastic two-dimensional flows is based on a hybrid centered-difference WENO method and a ghost-fluid approach at the interface. The authors employ a fourth-order centered-difference stencil away from discontinuities that requires no explicit calculation of the local hyperbolic characteristic information. As a result, the scheme is constructed in a general way to allow for possibly different constitutive relations. In the same spirit, a conventional third-order WENO scheme and a ghost-fluid method are applied in [2] to actual three-dimensional simulations of hyperelastic and plastic impacts and penetration with adaptive mesh refinement. It is known that approximate Riemann solvers for such problems may lead to inaccurate intermediate states as noted in [23,4]. However, these local inaccuracies do not seem to significantly pollute the solution when compared to exact test cases [14,11,16].

Hence, the typical features of integration schemes for Eulerian formulations of the hyperelastic conservation laws are: i) tracking of internal boundaries by a level set function; ii) approximate Riemann solver to compute numerical fluxes; iii) ghost-material approach to compute numerical fluxes at the material interface. In this respect, the present study details a twofold contribution to the simulation of complex three-dimensional hyperelastic phenomena. Firstly, we show under usual assumptions that the hyperelastic neohookean model employed satisfies the necessary conditions for hyperbolicity by explicitly computing the analytic wave speeds of small perturbations. Secondly, we simplify the computations of the numerical fluxes at the material interface such that no ghost material is defined and no mixture model is needed to obtain a non-oscillatory scheme, extending to three space dimensions the method presented in [16]. Thanks to this method, we are able to explicitly determine the internal boundary conditions modeling shock–bubble interactions, three-dimensional impacts and rebounds of hyperelastic materials immersed in a fluid.

2. The model

This model was already discussed in [15,26,27,24,7,11]. We follow here the formulation presented in [16] where a neo-hookean model was investigated and extend it to three dimensions.

2.1. Forward and backward characteristics

Let $\Omega_0 \subset \mathbb{R}^3$ be the reference (or initial) configuration of a continuous medium and $\Omega_t \subset \mathbb{R}^3$ the deformed configuration at time t. In order to describe the evolution of this medium in the Lagrangian frame we define the forward characteristics $X(\xi,t)$ as the image at time t in the deformed configuration of a material point ξ belonging to the initial configuration, i.e., $X : \Omega_0 \times [0,T] \longrightarrow \Omega_t$, $(\xi,t) \mapsto X(\xi,t)$ (see Fig. 1). The corresponding Eulerian velocity field u is defined as $u : \Omega_t \times [0,T] \longrightarrow \mathbb{R}^3$, $(x,t) \mapsto u(x,t)$ where

$$\begin{cases} X_t(\xi,t) = u(X(\xi,t),t) \\ X(\xi,0) = \xi \end{cases} \tag{1}$$

To describe the continuous medium in the Eulerian frame, we introduce the backward characteristics $Y(x,t)$ (see [7]) that for a time t and a point x in the deformed configuration, gives the corresponding initial point ξ in the initial configuration, i.e., $Y : \Omega_t \times [0,T] \longrightarrow \Omega_0$, $(x,t) \mapsto Y(x,t)$ (see Fig. 1). Since $Y(X(\xi,t),t) = \xi$, differentiating with respect to time and space in turn we have:

$$\begin{cases} Y_t + u \cdot \nabla_x Y = 0 \\ \qquad Y(x,0) = x \end{cases} \tag{2}$$

and

$$[\nabla_\xi X(\xi,t)] = [\nabla_x Y(x,t)]^{-1}. \tag{3}$$

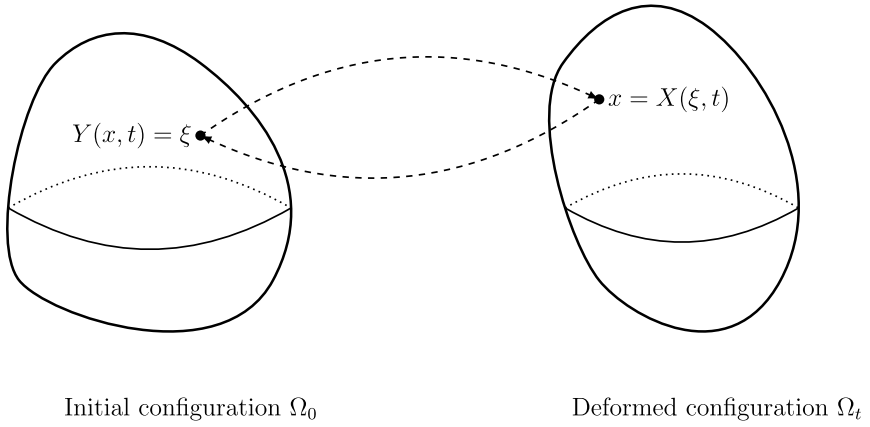


Fig. 1. Forward and backward characteristics.

The relation (2) is the Eulerian equivalent of the characteristic equation (1). In addition, equation (3) allows to compute the gradient of the deformation in the Eulerian frame via Y.

2.2. Eulerian model

The local form of the governing equations of mass, momentum and energy conservation in the deformed configuration Ω_t can be written as

$$\begin{cases} \rho_t + \mathrm{div}_x(\rho u) = 0 \\ (\rho u)_t + \mathrm{div}_x(\rho u \otimes u - \sigma) = 0 \\ (\rho e)_t + \mathrm{div}_x(\rho e u - \sigma^T u) = 0 \end{cases} \tag{4}$$

The physical variables are the density $\rho(x,t)$, the velocity $u(x,t)$, the total energy per unit mass $e(x,t)$ and the Cauchy stress tensor in the physical domain $\sigma(x,t)$. To close these systems a constitutive law is needed to detail the relationship between the stress tensors and the other physical variables.

2.3. Hyperelastic models

The classical results of this section can be found in the textbook [18]. Let us define $\varepsilon = e - \frac{1}{2}|u|^2$ the internal energy per unit mass. In the hyperelastic context, ε is a function of the deformation tensor $\nabla_\xi X$ and the entropy s.

The energy has to be Galilean invariant and we focus in this paper on the isotropic case. It can be proved that the material is Galilean invariant and isotropic if, and only if, ε is expressed as a function of the invariants of the right Cauchy–Green tensor $C(\xi,t) = [\nabla_\xi X]^T[\nabla_\xi X]$ or equivalently of the invariants of the left Cauchy–Green tensor $B(\xi,t) = [\nabla_\xi X][\nabla_\xi X]^T$. The three dimensional invariants often considered in the literature are $\mathrm{Tr}(\cdot)$, $\mathrm{Tr}(\mathrm{Cof}(\cdot)) = (\mathrm{Tr}(\cdot)^2 - \mathrm{Tr}(\cdot^2))/2$ and $\mathrm{Det}(\cdot)$.

We assume that ε is the sum of $\varepsilon_{\mathrm{vol}}$, a term depending on volume variation and entropy, and $\varepsilon_{\mathrm{iso}}$ a term accounting for isochoric deformation. Hence the internal energy is given by

$$\varepsilon = \varepsilon_{\mathrm{vol}}(\rho, s) + \varepsilon_{\mathrm{iso}}(\mathrm{Tr}(\overline{B}), \mathrm{Tr}(\overline{B}^{-1})) \tag{5}$$

where in three dimensions we have

$$\overline{B}(x,t) = [\nabla_x Y]^{-1}[\nabla_x Y]^{-T}/J^{\frac{2}{3}}(x,t) \qquad J(x,t) = \det([\nabla_x Y])^{-1} \tag{6}$$

Tensor $\overline{B}$ accounts for isochoric deformations since $\det(\overline{B}) = 1$. In general the term relative to an isochoric transformation may also depend on entropy. Here, we will limit the discussion to materials where the isochoric term is independent of the entropy, as in the case of idealized crystals (metals, ceramic).

The Cauchy stress tensor $\sigma(x,t)$ is then given by (see [18] for the details)

$$\sigma(x,t) = -\rho^2 \frac{\partial \varepsilon_{\mathrm{vol}}}{\partial \rho}\Big|_s(\rho, s) I + 2J^{-1}\left(\overline{\sigma}_{\mathrm{iso}} - \frac{\mathrm{Tr}(\overline{\sigma}_{\mathrm{iso}})}{3} I\right) \tag{7}$$

where

$$\overline{\sigma}_{\mathrm{iso}} = \frac{\partial \varepsilon_{\mathrm{iso}}}{\partial \alpha}\overline{B} - \frac{\partial \varepsilon_{\mathrm{iso}}}{\partial \beta}\overline{B}^{-1} \tag{8}$$

and α, β denote the first and second arguments of $\varepsilon_{\mathrm{iso}}$, respectively.

2.4. Overall model

Together with equations of mass, momentum and energy conservation (4), the additional equation (2) is required in order to record the deformation in the Eulerian frame. However, since σ will directly depend on $\nabla_x Y$ (5)–(7) we take the gradient of (2) as a governing equation and obtain the system in conservative form

$$\begin{cases} \rho_t + \operatorname{div}_x(\rho u) = 0 \\ (\rho u)_t + \operatorname{div}_x(\rho u \otimes u - \sigma) = 0 \\ (\nabla_x Y)_t + \nabla_x(u \cdot \nabla_x Y) = 0 \\ (\rho e)_t + \operatorname{div}_x(\rho e u - \sigma^T u) = 0 \end{cases} \tag{9}$$

where some fluxes of $\nabla_x Y$ are zero (see equation (13)). The initial density $\rho(x,0)$, the initial velocity $u(x,0)$, the initial total energy $e(x,0)$ and $\nabla_x Y(x,0) = I$ are given together with appropriate boundary conditions. This system is known in the literature as the inverse deformation gradient formulation.

We choose a general constitutive law that models gas, fluids and elastic solids. The internal energy per unit mass $\varepsilon = e - \frac{1}{2}|u|^2$ is defined as

$$\varepsilon(\rho, s, \nabla_x Y) = \overbrace{\underbrace{\frac{\kappa(s)}{\gamma - 1}\left(\frac{1}{\rho} - b\right)^{1-\gamma} - a\rho}_{\text{van der Waals gas}} + \frac{p_\infty}{\rho}}^{\text{stiffened gas}} + \overbrace{\frac{\chi}{\rho_0}(\operatorname{Tr}(\overline{B}) - 3)}^{\text{neohookean elastic solid}} \tag{10}$$

where $\overline{B}$ is defined in (6). We obtain according to (7)

$$\sigma(\rho, s, \nabla_x Y) = -p(\rho, s) I + 2\chi J^{-1}\left(\overline{B} - \frac{\operatorname{Tr}(\overline{B})}{3} I\right) \tag{11}$$

where

$$p(\rho, s) = -p_\infty - a\rho^2 + \kappa(s)\left(\frac{1}{\rho} - b\right)^{-\gamma} \tag{12}$$

Here $\kappa(s) = \exp\left(\frac{s}{c_v}\right)$ and c_v, γ, p_∞, a, b, χ are positive constants that characterize a given material. Parameters a and b correspond to the van der Waals parameters, p_∞ accounts for fluid or solid materials where intermolecular forces are present (see for example [14,11]). The last term in the energy expression models a neohookean elastic solid where the constant χ is the shear elastic modulus. For very large deformations, more complete models (Mooney-Rivlin, Ogden) take into account an additional invariant in the energy function in three dimensions. Without loosing in generality, here we stick to a neohookean model as it leads to simpler expressions in the following developments.

3. Numerical scheme

Let $x = (x_1, x_2, x_3)$ be the coordinates in the canonical basis of $\mathbb{R}^3$, $u = (u_1, u_2, u_3)$ the velocity components, $Y^i_{,j}$ the components of the tensor $[\nabla_x Y]$ and σ^{ij} the components of the stress tensor σ. Equations (9) become

$$\begin{pmatrix} \rho \\ \rho u_1 \\ \rho u_2 \\ \rho u_3 \\ Y^1_{,1} \\ Y^2_{,1} \\ Y^3_{,1} \\ Y^1_{,2} \\ Y^2_{,2} \\ Y^3_{,2} \\ Y^1_{,3} \\ Y^2_{,3} \\ Y^3_{,3} \\ \rho e \end{pmatrix}_{,t} + \begin{pmatrix} \rho u_1 \\ \frac{(\rho u_1)^2}{\rho} - \sigma^{11} \\ \frac{\rho u_1 \rho u_2}{\rho} - \sigma^{21} \\ \frac{\rho u_1 \rho u_3}{\rho} - \sigma^{31} \\ \frac{\rho u_1 Y^1_{,1} + \rho u_2 Y^1_{,2} + \rho u_3 Y^1_{,3}}{\rho} \\ \frac{\rho u_1 Y^2_{,1} + \rho u_2 Y^2_{,2} + \rho u_3 Y^2_{,3}}{\rho} \\ \frac{\rho u_1 Y^3_{,1} + \rho u_2 Y^3_{,2} + \rho u_3 Y^3_{,3}}{\rho} \\ 0 \\ 0 \\ 0 \\ 0 \\ 0 \\ \frac{\rho u_1 \rho e - (\sigma^{11}\rho u_1 + \sigma^{21}\rho u_2 + \sigma^{31}\rho u_3)}{\rho} \end{pmatrix}_{,1} + \begin{pmatrix} \rho u_2 \\ \frac{\rho u_1 \rho u_2}{\rho} - \sigma^{12} \\ \frac{(\rho u_2)^2}{\rho} - \sigma^{22} \\ \frac{\rho u_2 \rho u_3}{\rho} - \sigma^{32} \\ 0 \\ 0 \\ 0 \\ \frac{\rho u_1 Y^1_{,1} + \rho u_2 Y^1_{,2} + \rho u_3 Y^1_{,3}}{\rho} \\ \frac{\rho u_1 Y^2_{,1} + \rho u_2 Y^2_{,2} + \rho u_3 Y^2_{,3}}{\rho} \\ \frac{\rho u_1 Y^3_{,1} + \rho u_2 Y^3_{,2} + \rho u_3 Y^3_{,3}}{\rho} \\ 0 \\ 0 \\ 0 \\ \frac{\rho u_2 \rho e - (\sigma^{12}\rho u_1 + \sigma^{22}\rho u_2 + \sigma^{32}\rho u_3)}{\rho} \end{pmatrix}_{,2} + \begin{pmatrix} \rho u_3 \\ \frac{\rho u_1 \rho u_3}{\rho} - \sigma^{13} \\ \frac{\rho u_2 \rho u_3}{\rho} - \sigma^{23} \\ \frac{(\rho u_3)^2}{\rho} - \sigma^{33} \\ 0 \\ 0 \\ 0 \\ 0 \\ 0 \\ 0 \\ \frac{\rho u_1 Y^1_{,1} + \rho u_2 Y^1_{,2} + \rho u_3 Y^1_{,3}}{\rho} \\ \frac{\rho u_1 Y^2_{,1} + \rho u_2 Y^2_{,2} + \rho u_3 Y^2_{,3}}{\rho} \\ \frac{\rho u_1 Y^3_{,1} + \rho u_2 Y^3_{,2} + \rho u_3 Y^3_{,3}}{\rho} \\ \frac{\rho u_3 \rho e - (\sigma^{13}\rho u_1 + \sigma^{23}\rho u_2 + \sigma^{33}\rho u_3)}{\rho} \end{pmatrix}_{,3} = \begin{pmatrix} 0 \\ 0 \\ 0 \\ 0 \\ 0 \\ 0 \\ 0 \\ 0 \\ 0 \\ 0 \\ 0 \\ 0 \\ 0 \\ 0 \end{pmatrix} \tag{13}$$

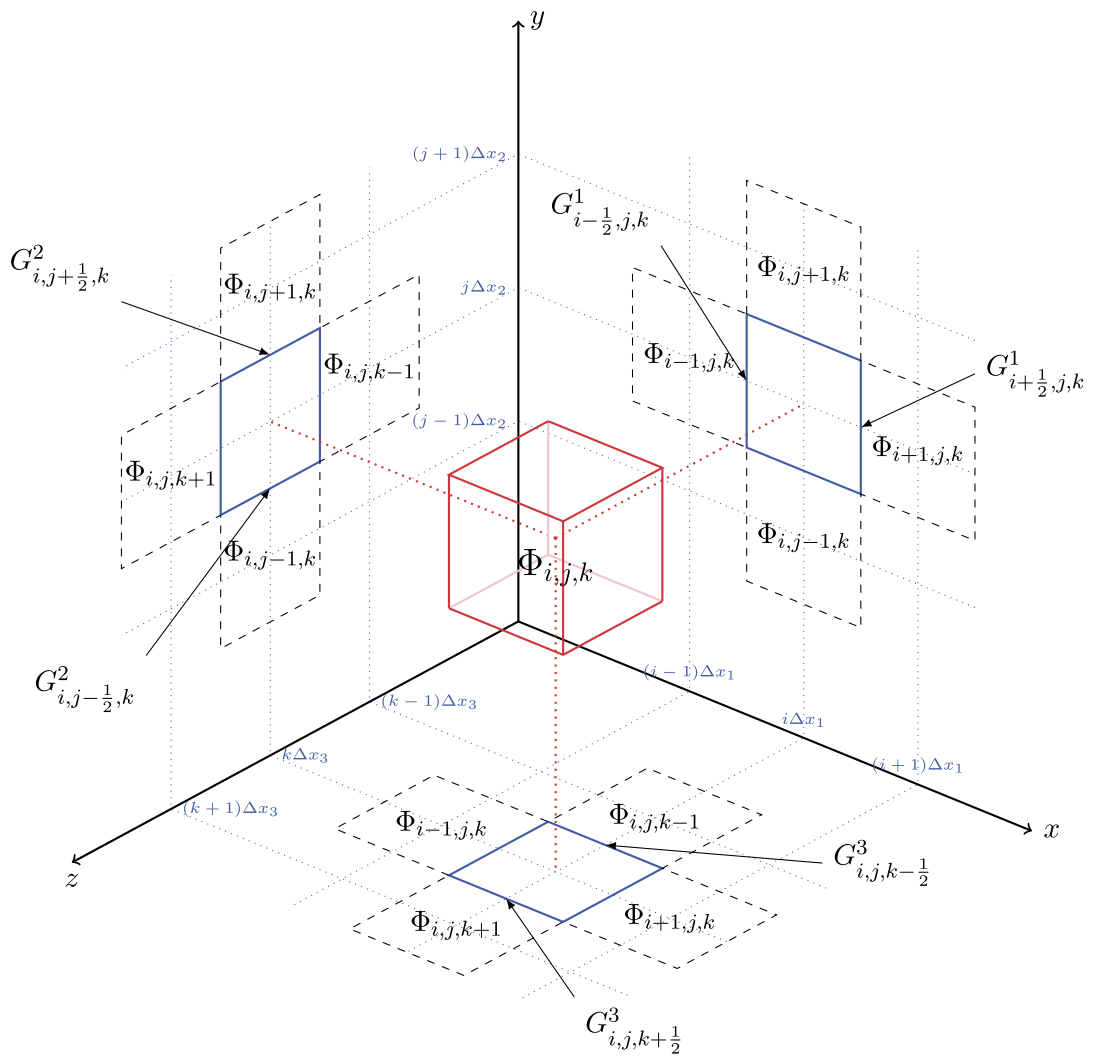


Fig. 2. Discretization on the control volume $\Omega_{i,j,k}$. Two-dimensional sections of the computational cell are projected on planes (xy), (yz) and (zx).

This system can be written in the compact form

$$\Phi_t + (G^1(\Phi))_{,1} + (G^2(\Phi))_{,2} + (G^3(\Phi))_{,3} = 0 \tag{14}$$

We discretize (14) with a finite volume method on a Cartesian mesh. Let Δx_i be the grid spacing in the x_i direction and $\Omega_{i,j,k}$ the control volume centered at the node $(i\Delta x_1, j\Delta x_2, k\Delta x_3)$. The semi-discretization in space of (14) on $\Omega_{i,j,k}$ gives

$$(\Phi_{i,j,k})_t + \frac{G^1_{i+1/2,j,k} - G^1_{i-1/2,j,k}}{\Delta x_1} + \frac{G^2_{i,j+1/2,k} - G^2_{i,j-1/2,k}}{\Delta x_2} + \frac{G^3_{i,j,k+1/2} - G^3_{i,j,k-1/2}}{\Delta x_3} = 0 \tag{15}$$

where $\Phi_{i,j,k}$ is the value of the conservative variable integrated on $\Omega_{i,j,k}$. In Fig. 2 are shown sections in two dimensions of the three-dimensional computational cell projected on their respective parallel planes.

The fluxes in (15) will be computed by approximate one-dimensional Riemann solvers in the direction orthogonal to the cell sides of the Cartesian mesh. Therefore, we have

$$G^1_{i-1/2,j,k} \approx \mathcal{F}(\Phi_{i-1,j,k}; \Phi_{i,j,k}) \qquad G^1_{i+1/2,j,k} \approx \mathcal{F}(\Phi_{i,j,k}; \Phi_{i+1,j,k}) \tag{16}$$

$$G^2_{i,j-1/2,k} \approx \mathcal{F}(\Phi_{i,j-1,k}; \Phi_{i,j,k}) \qquad G^2_{i,j+1/2,k} \approx \mathcal{F}(\Phi_{i,j,k}; \Phi_{i,j+1,k}) \tag{17}$$

$$G^3_{i,j,k-1/2} \approx \mathcal{F}(\Phi_{i,j,k-1}; \Phi_{i,j,k})1 \qquad G^3_{i,j,k+1/2} \approx \mathcal{F}(\Phi_{i,j,k}; \Phi_{i,j,k+1}) \tag{18}$$

where $\mathcal{F}(\cdot\,;\,\cdot)$ is a numerical flux function that will be specified in the following.

The fluxes in (13) are the same in the three spatial directions. Let us consider the one-dimensional problem in the x_1 direction

$$\Phi_t + (G^1(\Phi))_{,1} = 0 \tag{19}$$

where we have $(Y^i_{,2})_t = (Y^i_{,3})_t = 0$. These equations introduce six characteristics in (19) whose speeds are 0. This means also that $Y^i_{,2}$ and $Y^i_{,3}$ are just constant parameters in the other equations of the system. Therefore, in the next sections we focus on the wave structure of the following one-dimensional problem

$$\Psi_t + (F(\Psi))_{,1} = 0 \tag{20}$$

where

$$\Psi = \begin{pmatrix} \rho \\ \rho u_1 \\ \rho u_2 \\ \rho u_3 \\ Y^1_{,1} \\ Y^2_{,1} \\ Y^3_{,1} \\ \rho e \end{pmatrix} \qquad F(\Psi) = \begin{pmatrix} \rho u_1 \\ \frac{(\rho u_1)^2}{\rho} - \sigma^{11} \\ \frac{\rho u_1 \rho u_2}{\rho} - \sigma^{21} \\ \frac{\rho u_1 \rho u_3}{\rho} - \sigma^{31} \\ \frac{\rho u_1 Y^1_{,1} + \rho u_2 Y^1_{,2} + \rho u_3 Y^1_{,3}}{\rho} \\ \frac{\rho u_1 Y^2_{,1} + \rho u_2 Y^2_{,2} + \rho u_3 Y^2_{,3}}{\rho} \\ \frac{\rho u_1 Y^3_{,1} + \rho u_2 Y^3_{,2} + \rho u_3 Y^3_{,3}}{\rho} \\ \frac{\rho u_1 \rho e - (\sigma^{11}\rho u_1 + \sigma^{21}\rho u_2 + \sigma^{31}\rho u_3)}{\rho}. \end{pmatrix}$$

4. Characteristic speeds

In this section we extend in three dimensions the criterion given in [16] to analytically compute the wave speeds. Also, we prove that when we consider a neohookean constitutive law, the wave speeds are real for any deformation under usual assumptions.

4.1. General case

The governing equations (20) are closed with the constitutive law (5)–(7) which defines σ as a non-linear function of the unknowns. In this adiabatic and inviscid model, it can be shown that entropy is just transported along the characteristics for smooth solutions. Since the wave velocities are locally defined by infinitesimal smooth variations of the conservative variables Ψ, the energy equation can be simply replaced by $s_t + u \cdot \nabla s = 0$. Thus, instead of (20), we study the following quasi-linear system:

$$\begin{pmatrix} \rho \\ \rho u_1 \\ \rho u_2 \\ \rho u_3 \\ Y^1_{,1} \\ Y^2_{,1} \\ Y^3_{,1} \\ s \end{pmatrix}_{,t} + \begin{pmatrix} 0 & 1 & 0 & 0 & 0 & 0 & 0 & 0 \\ -\frac{(\rho u_1)^2}{\rho^2} & \frac{2\rho u_1}{\rho} & 0 & 0 & -\sigma^{11}_{,1} & -\sigma^{11}_{,2} & -\sigma^{11}_{,3} & -\sigma^{11}_{,s} \\ -\frac{\rho u_1 \rho u_2}{\rho^2} & \frac{\rho u_2}{\rho} & \frac{\rho u_1}{\rho} & 0 & -\sigma^{21}_{,1} & -\sigma^{21}_{,2} & -\sigma^{21}_{,3} & -\sigma^{21}_{,s} \\ -\frac{\rho u_1 \rho u_3}{\rho^2} & \frac{\rho u_3}{\rho} & 0 & \frac{\rho u_1}{\rho} & -\sigma^{31}_{,1} & -\sigma^{31}_{,2} & -\sigma^{31}_{,3} & -\sigma^{31}_{,s} \\ -\frac{\rho u_1 Y^1_{,1} + \rho u_2 Y^1_{,2} + \rho u_3 Y^1_{,3}}{\rho^2} & \frac{Y^1_{,1}}{\rho} & \frac{Y^1_{,2}}{\rho} & \frac{Y^1_{,3}}{\rho} & \frac{\rho u_1}{\rho} & 0 & 0 & 0 \\ -\frac{\rho u_1 Y^2_{,1} + \rho u_2 Y^2_{,2} + \rho u_3 Y^2_{,3}}{\rho^2} & \frac{Y^2_{,1}}{\rho} & \frac{Y^2_{,1}}{\rho} & \frac{Y^2_{,3}}{\rho} & 0 & \frac{\rho u_1}{\rho} & 0 & 0 \\ -\frac{\rho u_1 Y^3_{,1} + \rho u_2 Y^3_{,2} + \rho u_3 Y^3_{,3}}{\rho^2} & \frac{Y^3_{,1}}{\rho} & \frac{Y^3_{,1}}{\rho} & \frac{Y^3_{,3}}{\rho} & 0 & 0 & \frac{\rho u_1}{\rho} & 0 \\ 0 & 0 & 0 & 0 & 0 & 0 & 0 & \frac{\rho u_1}{\rho} \end{pmatrix} \begin{pmatrix} \rho \\ \rho u_1 \\ \rho u_2 \\ \rho u_3 \\ Y^1_{,1} \\ Y^2_{,1} \\ Y^3_{,1} \\ s \end{pmatrix}_{,1} = \begin{pmatrix} 0 \\ 0 \\ 0 \\ 0 \\ 0 \\ 0 \\ 0 \\ 0 \end{pmatrix} \tag{21}$$

where $\sigma^{ij}_{,1}$, $\sigma^{ij}_{,2}$, $\sigma^{ij}_{,3}$, and $\sigma^{ij}_{,s}$ denote the derivative of σ^{ij} with respect to $Y^1_{,1}$, $Y^2_{,1}$, $Y^3_{,1}$ and s respectively. We denote by J_{ac} the matrix appearing in (21).

We introduce the notation

$$\Sigma = [\nabla\sigma][\nabla Y] := \begin{pmatrix} \sigma^{11}_{,1} & \sigma^{11}_{,2} & \sigma^{11}_{,3} \\ \sigma^{21}_{,1} & \sigma^{21}_{,2} & \sigma^{21}_{,3} \\ \sigma^{31}_{,1} & \sigma^{31}_{,2} & \sigma^{31}_{,3} \end{pmatrix} \begin{pmatrix} Y^1_{,1} & Y^1_{,2} & Y^1_{,3} \\ Y^2_{,1} & Y^2_{,2} & Y^2_{,3} \\ Y^3_{,1} & Y^3_{,2} & Y^3_{,3} \end{pmatrix} \tag{22}$$

The characteristic polynomial of J_{ac} can be written under the form

$$P(\lambda) = \frac{(\lambda - u_1)^2}{\rho^3}((\rho(u_1 - \lambda)^2)^3 + \mathrm{Tr}(\Sigma)(\rho(u_1 - \lambda)^2)^2 + \mathrm{Tr}(\mathrm{Cof}((\Sigma))(\rho(u_1 - \lambda)^2) + \mathrm{Det}(\Sigma))$$

so that the eigenvalues of J_{ac} are

$$\Lambda^E = \left\{ u_1, u_1, u_1 \pm \sqrt{\frac{\alpha_1}{\rho}}, u_1 \pm \sqrt{\frac{\alpha_2}{\rho}}, u_1 \pm \sqrt{\frac{\alpha_3}{\rho}} \right\} \tag{23}$$

where α_1, α_2 and α_3 are the roots of the polynomial of third order

$$X^3 + \mathrm{Tr}(\Sigma)X^2 + \mathrm{Tr}(\mathrm{Cof}((\Sigma))X + \mathrm{Det}(\Sigma) = 0 \tag{24}$$

Therefore, the necessary conditions for system (20) to be hyperbolic are $\alpha_1 > 0, \alpha_2 > 0$ and $\alpha_3 > 0$. In [25] it is shown that these conditions are also sufficient to ensure that a complete system of eigenvectors of the Jacobian matrix exists.

Roots of third order polynomial

With the change of variables $X = Z - \mathrm{Tr}(\Sigma)/3$, equation (24) reduces to

$$Z^3 + \mathcal{P}Z + \mathcal{Q} = 0 \tag{25}$$

where

$$\mathcal{P} = \mathrm{Tr}(\mathrm{Cof}((\Sigma)) - \frac{\mathrm{Tr}(\Sigma)^2}{3} \qquad \mathcal{Q} = \frac{2\mathrm{Tr}(\Sigma)^3}{27} - \frac{\mathrm{Tr}(\Sigma)\mathrm{Tr}(\mathrm{Cof}((\Sigma))}{3} + \mathrm{Det}(\Sigma) \tag{26}$$

The three solutions are reals if $\Delta_{3D} = 4\mathcal{P}^3 + 27\mathcal{Q}^2 \leq 0$ (which implies $\mathcal{P} \leq 0$) and are given by

$$\alpha_k = 2\sqrt{\frac{-\mathcal{P}}{3}} \cos\left(\frac{1}{3} \arccos\left(-\mathrm{sign}(\mathcal{Q}) \sqrt{1 - \frac{\Delta_{3D}}{4\mathcal{P}^3}} \right) + \frac{2k\pi}{3} \right) - \frac{\mathrm{Tr}(\Sigma)}{3} \qquad k = 1, 2, 3 \tag{27}$$

Moreover, the α_i are positive if $\mathrm{Tr}(\Sigma) < 0$, $\mathrm{Tr}(\mathrm{Cof}((\Sigma)) > 0$ and $\mathrm{Det}(\Sigma) < 0$. In the particular case where $\Delta_{3D} = 0$ we obtain a solution of multiplicity two

$$\alpha_1 = \frac{3\mathcal{Q}}{\mathcal{P}} - \frac{\mathrm{Tr}(\Sigma)}{3} \qquad \alpha_2 = \alpha_3 = -\frac{3\mathcal{Q}}{2\mathcal{P}} - \frac{\mathrm{Tr}(\Sigma)}{3} \tag{28}$$

4.2. Hyperbolicity of the neohookean model

The internal energy ε with the neohookean model reads

$$\varepsilon = \varepsilon_{\mathrm{iso}}(\rho, s) + \frac{\chi}{\rho_0}(\mathrm{Tr}(\overline{B}) - 3) \tag{29}$$

Let A be

$$A_{ij} = (-1)^{i+j}(K_{1i}K_{1j} + K_{2i}K_{2j} + K_{3i}K_{3j}) \tag{30}$$

where

$$\begin{aligned}
K_{11} &= Y^2_{,2}Y^3_{,3} - Y^3_{,2}Y^2_{,3} & K_{21} &= Y^1_{,2}Y^3_{,3} - Y^3_{,2}Y^1_{,3} & K_{31} &= Y^1_{,2}Y^2_{,3} - Y^2_{,2}Y^1_{,3} \\
K_{12} &= Y^2_{,1}Y^3_{,3} - Y^3_{,1}Y^2_{,3} & K_{22} &= Y^1_{,1}Y^3_{,3} - Y^3_{,1}Y^1_{,3} & K_{32} &= Y^1_{,1}Y^2_{,3} - Y^2_{,1}Y^1_{,3} \\
K_{13} &= Y^2_{,1}Y^3_{,2} - Y^3_{,1}Y^2_{,2} & K_{23} &= Y^1_{,1}Y^3_{,2} - Y^3_{,1}Y^1_{,2} & K_{33} &= Y^1_{,1}Y^2_{,2} - Y^2_{,1}Y^1_{,2}
\end{aligned}$$

We can show that $J^{-1}\overline{B} = AJ^{\frac{1}{3}}$. Therefore the expression of the stress tensor σ (11) becomes

$$\sigma = -p(\rho, s)I + 2\chi J^{\frac{1}{3}} \left(A - \frac{\mathrm{Tr}(A)}{3} I \right) \tag{31}$$

Using the square of the sound speed $c^2(\rho, s) = \left.\frac{\partial p}{\partial \rho}\right|_s$, (22) changes into

$$\Sigma = \frac{2}{9}\chi J^{1/3} \begin{pmatrix} D_1 & D_2 J\beta_2 + 6A_{12} & D_2 J\beta_3 + 6A_{13} \\ 6A_{12} & -3\beta_2 J A_{12} - 9A_{11} & -3\beta_3 J A_{12} \\ 6A_{13} & -3\beta_2 J A_{13} & -3\beta_3 J A_{13} - 9A_{11} \end{pmatrix} - \rho c^2 \begin{pmatrix} 1 & 0 & 0 \\ 0 & 0 & 0 \\ 0 & 0 & 0 \end{pmatrix} \tag{32}$$

where

$$\begin{aligned}
D_1 &= -2A_{11} - 5A_{22} - 5A_{33} & D_2 &= -2A_{11} + A_{22} + A_{33} \\
\beta_2 &= K_{11}Y^1_{,2} - K_{21}Y^2_{,2} + K_{31}Y^3_{,2} & \beta_3 &= K_{11}Y^1_{,3} - K_{21}Y^2_{,3} + K_{31}Y^3_{,3}
\end{aligned}$$

and we have the relation $\beta_2 A_{12} + \beta_3 A_{13} = 0$.

Thus, it follows that

$$\mathrm{Tr}(\Sigma) = -\left(\rho c^2 + \frac{10}{9}\chi J^{\frac{1}{3}}(4A_{11} + A_{22} + A_{33})\right) \tag{33}$$

$$\mathrm{Tr}(\mathrm{Cof}(\Sigma)) = 4\chi J^{\frac{1}{3}}\left(A_{11}\rho c^2 + \frac{1}{9}\chi J^{\frac{1}{3}}(\mathcal{C}_1 + 11A_{11}^2 + 5A_{11}(A_{22} + A_{33}))\right) \tag{34}$$

$$\det(\Sigma) = -(2\chi J^{\frac{1}{3}})^2 A_{11}\left(A_{11}\rho c^2 + \frac{2}{9}\chi J^{\frac{1}{3}}\mathcal{C}_1\right) \tag{35}$$

where

$$\mathcal{C}_1 = 2A_{11}^2 + (A_{12})^2 + (A_{13})^2 + 5(A_{11}A_{22} - (A_{12})^2 + A_{11}A_{33} - (A_{13})^2)$$

We have that $\mathcal{C}_1 \geq 0$ because

$$A_{11}A_{22} - (A_{12})^2 = (K_{12}K_{21} - K_{11}K_{22})^2 + (K_{12}K_{31} - K_{11}K_{32})^2 + (K_{22}K_{31} - K_{21}K_{32})^2 \geq 0$$
$$A_{11}A_{33} - (A_{13})^2 = (K_{13}K_{21} - K_{11}K_{23})^2 + (K_{13}K_{31} - K_{11}K_{33})^2 + (K_{23}K_{31} - K_{21}K_{33})^2 \geq 0$$

Since $A_{ii} \geq 0$, it follows that $\mathrm{Tr}(\Sigma) \leq 0, \mathrm{Tr}(\mathrm{Cof}((\Sigma)) > 0$ and $\mathrm{Det}(\Sigma) < 0$. The reduced parameters are then given by

$$\mathcal{P} = -\frac{1}{3}\left(\left(\rho c^2 - \frac{2}{9}\chi J^{\frac{1}{3}}\mathcal{C}_2\right)^2 + \frac{4}{3}(2\chi J^{\frac{1}{3}})^2\mathcal{C}_3\right) \tag{36}$$

$$\mathcal{Q} = -\frac{2}{27}\left(\rho c^2 - \frac{2}{9}\chi J^{\frac{1}{3}}\mathcal{C}_2\right)\left(\left(\rho c^2 - \frac{2}{9}\chi J^{\frac{1}{3}}\mathcal{C}_2\right)^2 + 2(2\chi J^{\frac{1}{3}})^2\mathcal{C}_3\right) \tag{37}$$

$$\Delta_{3D} = -\frac{1}{9}\left(\frac{4}{3}(2\chi J^{\frac{1}{3}})^2\mathcal{C}_3\right)^2\left(\left(\rho c^2 - \frac{2}{9}\chi J^{\frac{1}{3}}\mathcal{C}_2\right)^2 + \frac{16}{9}(2\chi J^{\frac{1}{3}})^2\mathcal{C}_3\right) \tag{38}$$

where

$$\mathcal{C}_2 = 7A_{11} - 5(A_{22} + A_{33}) \qquad \mathcal{C}_3 = (A_{12})^2 + (A_{13})^2 \geq 0$$

As $\mathcal{C}_3 \geq 0$ we obtain that $\mathcal{P} \leq 0$ and $\Delta_{3D} \leq 0$. Also, the sign of $\mathcal{Q}$ is equal to the sign of $\frac{2}{9}\chi J^{\frac{1}{3}}\mathcal{C}_2 - \rho c^2$.

This result shows that the necessary conditions for the neohookean model to be hyperbolic are satisfied, since the wave speeds given by (23) and (27) are real for any deformation, under the usual assumptions $c^2 > 0$ and $\chi \geq 0$.

4.3. Small deformations

We investigate the simplifications of the wave speeds for small deformations. In this case $\nabla Y \approx I$ and $A_{ij} = \delta_{ij}$. Hence, we have

$$\mathcal{C}_1 = 12 \qquad \mathcal{C}_2 = 3 \qquad \mathcal{C}_3 = 0$$

and (33)–(35) reduce to

$$\mathrm{Tr}(\Sigma) = -\left(\rho c^2 + \frac{20}{3}\chi\right) \leq 0$$
$$\mathrm{Tr}(\mathrm{Cof}(\Sigma)) = 4\chi\left(\rho c^2 + \frac{11}{3}\chi\right) \geq 0$$
$$\det(\Sigma) = -4\chi^2\left(\rho c^2 + \frac{8}{3}\chi\right) \leq 0$$

The reduced parameters are given by

$$\mathcal{P} = -\frac{1}{3}\left(\rho c^2 + \frac{2}{3}\chi\right)^2 \qquad \mathcal{Q} = -\frac{2}{27}\left(\rho c^2 + \frac{2}{3}\chi\right)^3 \qquad \Delta_{3D} = 0$$

Then, using (23) and (28), the waves speeds are given by

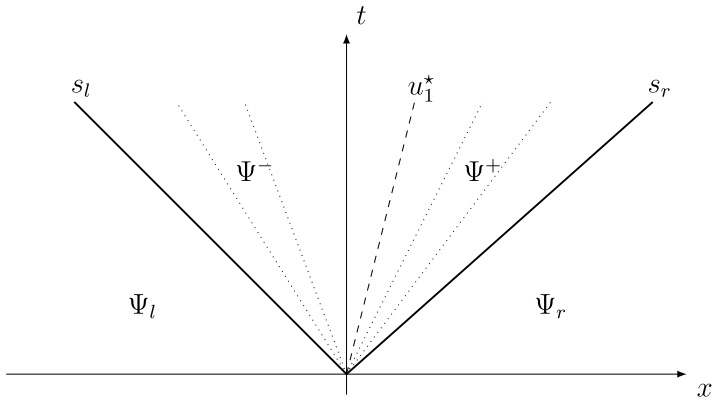


Fig. 3. HLLC solver wave pattern.

$$\Lambda^E = \left\{ u_1, u_1, u_1 \pm \sqrt{c^2 + \frac{4}{3}\frac{2\chi}{\rho}}, u_1 \pm \sqrt{\frac{2\chi}{\rho}}, u_1 \pm \sqrt{\frac{2\chi}{\rho}} \right\} \tag{39}$$

Therefore, in the small deformation limit the speeds corresponding to transverse waves coincide, as in the classical theory of linear elasticity.

5. Numerical flux

In this section we first introduce the HLLC solver employed for a single material. Then we specify the numerical flux for the multimaterial case.

5.1. HLLC solver

We consider equation (20) with the initial condition

$$\Psi(x, t=0) = \begin{cases} \Psi_l & \text{if } x \le 0 \\ \Psi_r & \text{if } x > 0. \end{cases} \tag{40}$$

The numerical flux function $\mathcal{F}(\Psi_l; \Psi_r)$ at the cell interface $x = 0$ is determined based on the solution of the HLLC [29] approximate Riemann problem, similarly to what is done in [14,16]. Even though the exact wave pattern involves seven distinct waves, see (23), the approximate solver approaches the solution using three waves (the contact discontinuity $u_1^\star$, the fastest leftward and rightward waves s_l and s_r), thus inducing only two intermediate states Ψ^- and Ψ^+ (see Fig. 3).

Let define the intermediate states Ψ^- and Ψ^+ and their related fluxes as

$$\Psi^- = \begin{pmatrix} \rho^- \\ \rho^- u_1^- \\ \rho^- u_2^- \\ \rho^- u_3^- \\ (Y^1_{,1})^- \\ (Y^2_{,1})^- \\ (Y^3_{,1})^- \\ (\rho e)^- \end{pmatrix} \qquad \mathcal{F}^- = \begin{pmatrix} \rho^- u_1^- \\ \rho^- (u_1^-)^2 - (\sigma^{11})^\star \\ \rho^- u_1^- u_2^- - (\sigma^{21})^\star \\ \rho^- u_1^- u_3^- - (\sigma^{31})^\star \\ u_1^- (Y^1_{,1})^- + u_2^- (Y^1_{,2})^- + u_3^- (Y^1_{,3})^- \\ u_1^- (Y^2_{,1})^- + u_2^- (Y^2_{,2})^- + u_3^- (Y^2_{,3})^- \\ u_1^- (Y^3_{,1})^- + u_2^- (Y^3_{,2})^- + u_3^- (Y^3_{,3})^- \\ u_1^- (\rho e)^- - ((\sigma^{11})^\star u_1^- + (\sigma^{21})^\star u_2^- + (\sigma^{31})^\star u_3^-) \end{pmatrix} \tag{41}$$

$$\Psi^+ = \begin{pmatrix} \rho^+ \\ \rho^+ u_1^+ \\ \rho^+ u_2^+ \\ \rho^+ u_3^+ \\ (Y^1_{,1})^+ \\ (Y^2_{,1})^+ \\ (Y^3_{,1})^+ \\ (\rho e)^+ \end{pmatrix} \qquad \mathcal{F}^+ = \begin{pmatrix} \rho^+ u_1^+ \\ \rho^+ (u_1^+)^2 - (\sigma^{11})^\star \\ \rho^+ u_1^+ u_2^+ - (\sigma^{21})^\star \\ \rho^+ u_1^+ u_3^+ - (\sigma^{31})^\star \\ u_1^+ (Y^1_{,1})^+ + u_2^+ (Y^1_{,2})^+ + u_3^+ (Y^1_{,3})^+ \\ u_1^+ (Y^2_{,1})^+ + u_2^+ (Y^2_{,2})^+ + u_3^+ (Y^2_{,3})^+ \\ u_1^+ (Y^3_{,1})^+ + u_2^+ (Y^3_{,2})^+ + u_3^+ (Y^3_{,3})^+ \\ u_1^+ (\rho e)^+ - ((\sigma^{11})^\star u_1^+ + (\sigma^{21})^\star u_2^+ + (\sigma^{31})^\star u_3^+) \end{pmatrix} \tag{42}$$

Here the stresses $(\sigma^{11})^\star$, $(\sigma^{21})^\star$ and $(\sigma^{31})^\star$ are independent unknowns.

The HLLC scheme is based on the assumption that every wave is a shock and therefore Rankine–Hugoniot relations give

$$\begin{cases} F(\Psi_r) - \mathcal{F}^+ = s_r(\Psi_r - \Psi^+) \\ \mathcal{F}^+ - \mathcal{F}^- = u_1(\Psi^+ - \Psi^-) \\ \mathcal{F}^- - F(\Psi_l) = s_l(\Psi^- - \Psi_l) \end{cases} \tag{43}$$

We introduce the notations

$$Q_l = F(\Psi_l) - s_l\Psi_l \qquad Q_r = F(\Psi_r) - s_r\Psi_r \tag{44}$$

and we denote by Q_l^i (respectively Q_r^i) the i-th component of Q_l (respectively Q_r). In the following, except when otherwise explicitly stated, we take $u_1^- = u_1^+ = u_1^\star$.

The Rankine–Hugoniot relations (43) lead to

$$\rho^- = \frac{Q_l^1}{u_1^- - s_l} \qquad \rho^+ = \frac{Q_r^1}{u_1^+ - s_r} \tag{45}$$

$$(Y_{,1}^1)^- = \frac{Q_l^5 - u_2^-(Y_{,2}^1)^- - u_3^-(Y_{,3}^1)^-}{u_1^- - s_l} \qquad (Y_{,1}^1)^+ = \frac{Q_r^5 - u_2^+(Y_{,2}^1)^+ - u_3^+(Y_{,3}^1)^+}{u_1^+ - s_r} \tag{46}$$

$$(Y_{,1}^2)^- = \frac{Q_l^6 - u_2^-(Y_{,2}^2)^- - u_3^-(Y_{,3}^2)^-}{u_1^- - s_l} \qquad (Y_{,1}^2)^+ = \frac{Q_r^6 - u_2^+(Y_{,2}^2)^+ - u_3^+(Y_{,3}^2)^+}{u_1^+ - s_r} \tag{47}$$

$$(Y_{,1}^3)^- = \frac{Q_l^7 - u_2^-(Y_{,2}^3)^- - u_3^-(Y_{,3}^3)^-}{u_1^- - s_l} \qquad (Y_{,1}^3)^+ = \frac{Q_r^7 - u_2^+(Y_{,2}^3)^+ - u_3^+(Y_{,3}^3)^+}{u_1^+ - s_r} \tag{48}$$

$$(\rho e)^- = \frac{Q_l^8 + (\sigma^{11})^\star u_1^- + (\sigma^{21})^\star u_2^- + (\sigma^{31})^\star u_3^-}{u_1^- - s_l} \qquad (\rho e)^+ = \frac{Q_r^8 + (\sigma^{11})^\star u_1^+ + (\sigma^{21})^\star u_2^+ + (\sigma^{31})^\star u_3^+}{u_1^+ - s_r} \tag{49}$$

The relations for the velocities $u_i^\pm$ and the stresses $(\sigma^{i1})^\star$ are linked and are described in the three following cases.

(1) In the case where both Ψ_l and Ψ_r are solid states ($\chi \neq 0$), all velocity and stress components are continuous across the contact discontinuity. Hence, it follows that

$$u_1^- = u_1^+ = u_1^\star = \frac{Q_l^2 - Q_r^2}{Q_l^1 - Q_r^1} \qquad (\sigma^{11})^\star = \frac{Q_l^2 Q_r^1 - Q_l^1 Q_r^2}{Q_l^1 - Q_r^1} \tag{50}$$

$$u_2^- = u_2^+ = u_2^\star = \frac{Q_l^3 - Q_r^3}{Q_l^1 - Q_r^1} \qquad (\sigma^{21})^\star = \frac{Q_l^3 Q_r^1 - Q_l^1 Q_r^3}{Q_l^1 - Q_r^1} \tag{51}$$

$$u_3^- = u_3^+ = u_3^\star = \frac{Q_l^4 - Q_r^4}{Q_l^1 - Q_r^1} \qquad (\sigma^{31})^\star = \frac{Q_l^4 Q_r^1 - Q_l^1 Q_r^4}{Q_l^1 - Q_r^1} \tag{52}$$

(2) When at least one of the states Ψ_l or Ψ_r is fluid ($\chi = 0$) or in the case where both Ψ_l and Ψ_r are solid states ($\chi \neq 0$) with a frictionless contact, we have that u_1 and σ^{11} are continuous. Hence, equation (50) is still verified. However since σ^{21} and σ^{31} vanish at the interface, the transverse velocities u_2 and u_3 can be discontinuous. It follows that equations (51)–(52) are replaced by

$$u_2^- = \frac{Q_l^3}{Q_l^1} \qquad u_2^+ = \frac{Q_r^3}{Q_r^1} \qquad (\sigma^{21})^\star = 0 \tag{53}$$

$$u_3^- = \frac{Q_l^4}{Q_l^1} \qquad u_3^+ = \frac{Q_r^4}{Q_r^1} \qquad (\sigma^{31})^\star = 0 \tag{54}$$

(3) If Ψ_l and Ψ_r are solid states ($\chi \neq 0$) relative to two different objects in frictionless contact, a rebound with material contact takes place when the normal velocities of the states Ψ_l and Ψ_r are such that $u_r > u_l$. In this case σ^{11}, σ^{21} and σ^{31} vanish and the velocities u_1, u_2 and u_3 are discontinuous. The stress components σ^{11}, σ^{21} and σ^{31} are negligible based on the hypothesis that when $u_r > u_l$, a tiny film of gas is instantaneously formed between the two solids at a negligible pressure compared to the stress in the elastic materials. Hence, equations (53)–(54) are still verified and equations (50) are replaced by

$$u_1^- = \frac{Q_l^2}{Q_l^1} \qquad u_1^+ = \frac{Q_r^2}{Q_r^1} \qquad (\sigma^{11})^\star = 0 \tag{55}$$

Similarly to [16], from equations (43) we consistently obtain

$$(Y^i_{,2})^{\pm} = \frac{(Y^i_{,2})_l + (Y^i_{,2})_r}{2}$$

and

$$(Y^i_{,3})^{\pm} = \frac{(Y^i_{,3})_l + (Y^i_{,3})_r}{2}.$$

Finally, the robustness of the scheme is strongly influenced by the estimation of s_l and s_r. We use the estimate presented in [8] which is a simple way to obtain robust speed estimates:

$$s_l = \min((u_1 - \lambda)_l, (u_1 - \lambda)_r) \qquad s_r = \max((u_1 + \lambda)_l, (u_1 + \lambda)_r).$$

where $\lambda = \sqrt{\frac{\max \alpha_i}{\rho}}$.

Equations (45)–(55) completely define the intermediate states $\Psi^{\pm}$ and their associated fluxes $\mathcal{F}^{\pm}$. The numerical flux at the cell interface $x = 0$ is then given by

$$\mathcal{F}(\Psi_l; \Psi_r) = \begin{cases} F(\Psi_l) & \text{if} \quad 0 \le s_l \\ \mathcal{F}^- & \text{if} \quad s_l \le 0 \le u_1^\star \\ \mathcal{F}^+ & \text{if} \quad u_1^\star \le 0 \le s_r \\ F(\Psi_r) & \text{if} \quad s_r \le 0 \end{cases} \tag{56}$$

where F is defined in (20).

Finally, the waves corresponding to the degenerate characteristics in $Y^i_{,2}$ and $Y^i_{,3}$ do not contribute to the numerical flux in the direction 1. The variables $Y^i_{,2}$ and $Y^i_{,3}$ are updated in time when the fluxes in the directions 2 and 3, respectively, are computed.

5.2. Multimaterial solver

The multimaterial solver is detailed in one dimension for sake of clarity and is the same as in [16]. In three dimensions we use the same method in all directions. We consider a case where the interface separating materials with different constitutive laws is located between the cell centers $k-1$ and k. The main idea of the multimaterial solver is that, instead of (56) we take

$$\mathcal{F}^l_{k-1/2} = \mathcal{F}^- \qquad \mathcal{F}^r_{k-1/2} = \mathcal{F}^+ \tag{57}$$

(see Fig. 4, equations (41) and (42)).

As for ghost-fluid methods, the scheme is locally non-conservative since $\mathcal{F}^- \neq \mathcal{F}^+$, but it is consistent since $\mathcal{F}^{\pm}$ are regular enough functions of the states to the left and to the right of the interface and $\mathcal{F}^+ = \mathcal{F}^-$ when those states are identical. In [16] it is shown that the error in conservation is negligible as the number of cell interfaces for which a non-conservative numerical flux is employed is always negligible compared to the total number of mesh cells.

A special care is needed at the multimaterial interface. To avoid the singularity due to the discontinuity of Y and to keep the interface sharp, the computation of $(Y^i_{,2})^{\pm}$ and $(Y^i_{,3})^{\pm}$ is one-sided:

$$(Y^i_{,2})^- = (Y^i_{,2})_l \qquad (Y^i_{,2})^+ = (Y^i_{,2})_r \tag{58}$$

$$(Y^i_{,3})^- = (Y^i_{,3})_l \qquad (Y^i_{,3})^+ = (Y^i_{,3})_r \tag{59}$$

This can be seen as an extension by continuity of $Y^i_{,2}$ and $Y^i_{,3}$ relative to each material.

5.3. Extension to second-order in each space direction

The scheme is extended to second-order accuracy using a piecewise-linear slope reconstruction in space, with minmod limiter. For the cells separated by the multimaterial interface, the stencil used to compute the slopes is smaller. We calculate these slopes using the corresponding intermediate state of the multimaterial Riemann problem. For example, if cells $k-1$ and k do not belong to the same medium, the slope of cell $k-1$ is computed using Ψ_{k-2}, Ψ_{k-1} and the intermediate state to the left of the contact discontinuity. This state is determined thanks to the solution of an approximate Riemann problem between Ψ_{k-1} and Ψ_k, without slope reconstruction.

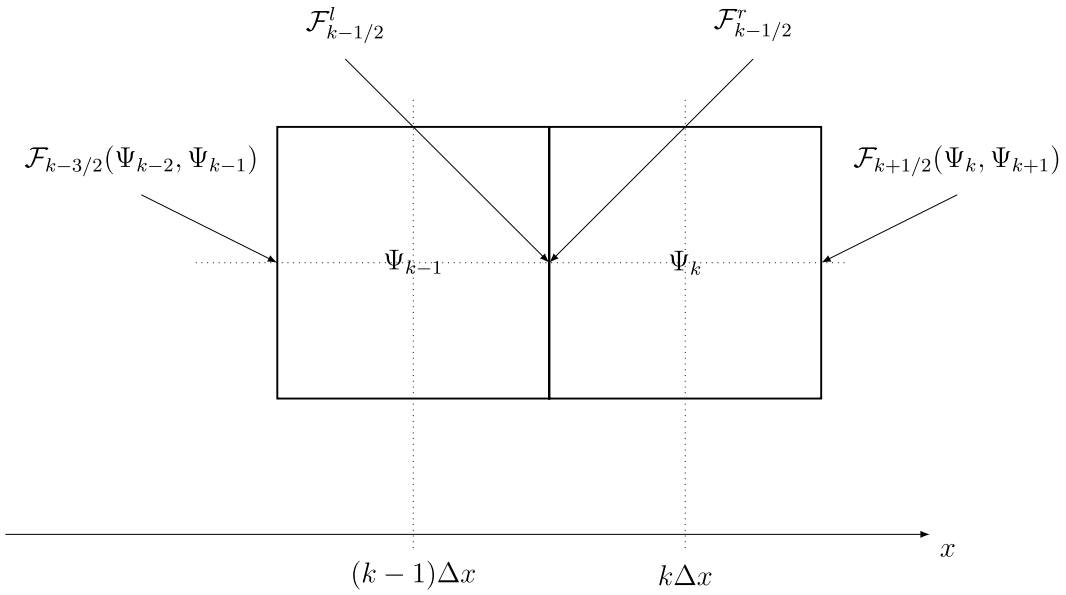


Fig. 4. Fluxes at the material discontinuity.

Table 1
Test cases description.

TC	Media	ρ [kg m^{-3}]	u_1 [m s^{-1}]	p [Pa]	γ	a	b	p_∞ [Pa]	χ [Pa]
1	Air (pre-shock)	1.225	0	101 325	1.4	0	0	0	0
	Air (post-shock)	1.6861	−113.534	159 059					
	Helium	0.2228	0	101 325	1.648	0	0	0	0
2	Water (pre-shock)	1000	0	10^5	4.4	0	0	$6 \cdot 10^8$	0
	Water (post-shock)	1230	−432.69	10^9					
	Air	1.2	0	10^5	1.4	5	10^{-3}	0	0
3	Copper (plate)	8900	0	10^5	4.22	0	0	$3.42 \cdot 10^{10}$	$5 \cdot 10^{10}$
4	Copper (projectile)	8900	u_p	10^5					
5	Air	1	0	10^5	1.4	0	0	0	0
6									

5.4. Interface advection and time integration

Coherently with a fully Eulerian approach, a level set function is used to follow the interface separating different materials. The level set function is transported with the velocity field by the equation:

$$\varphi_t + u \cdot \nabla\varphi = 0 \tag{60}$$

This equation is approximated with a WENO 5 scheme [19].

The conservation equations and the interface advection are explicitly integrated in time by a Runge–Kutta 2 scheme. The interface position is advected using the material velocity field. For numerical stability, the integration step is limited by the fastest characteristics over the grid points. Hence, the interface position will belong to the same interval between two grid points for more than one time step. When the physical interface overcomes a grid point, the corresponding conservative variables, say Ψ_k, do not correspond anymore to the material present at that grid point before the integration step. When the physical interface moves to the right, then we take $\Psi_k = \Psi^-$, whereas if it moves to the left $\Psi_k = \Psi^+$. In three dimensions this is done direction by direction taking the resulting average for the conservative variables.

6. Numerical results

We show in this section three-dimensional shock–bubble interactions and impacts in air. In particular, we simulate elastic rebounds in two and three dimensions. Computation are performed with an MPI parallel code.

Table 1 shows the material properties and initial conditions relative to each test case.

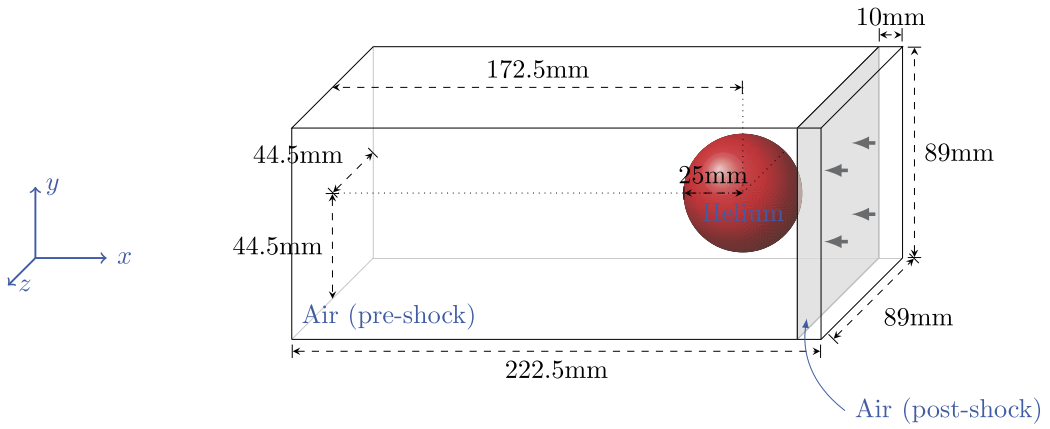


Fig. 5. Sketch of the initial configuration for the shock–bubble interaction TC1. The computational domain is $[247.5, 470] \times [0, 89] \times [0, 89]$ mm^3.

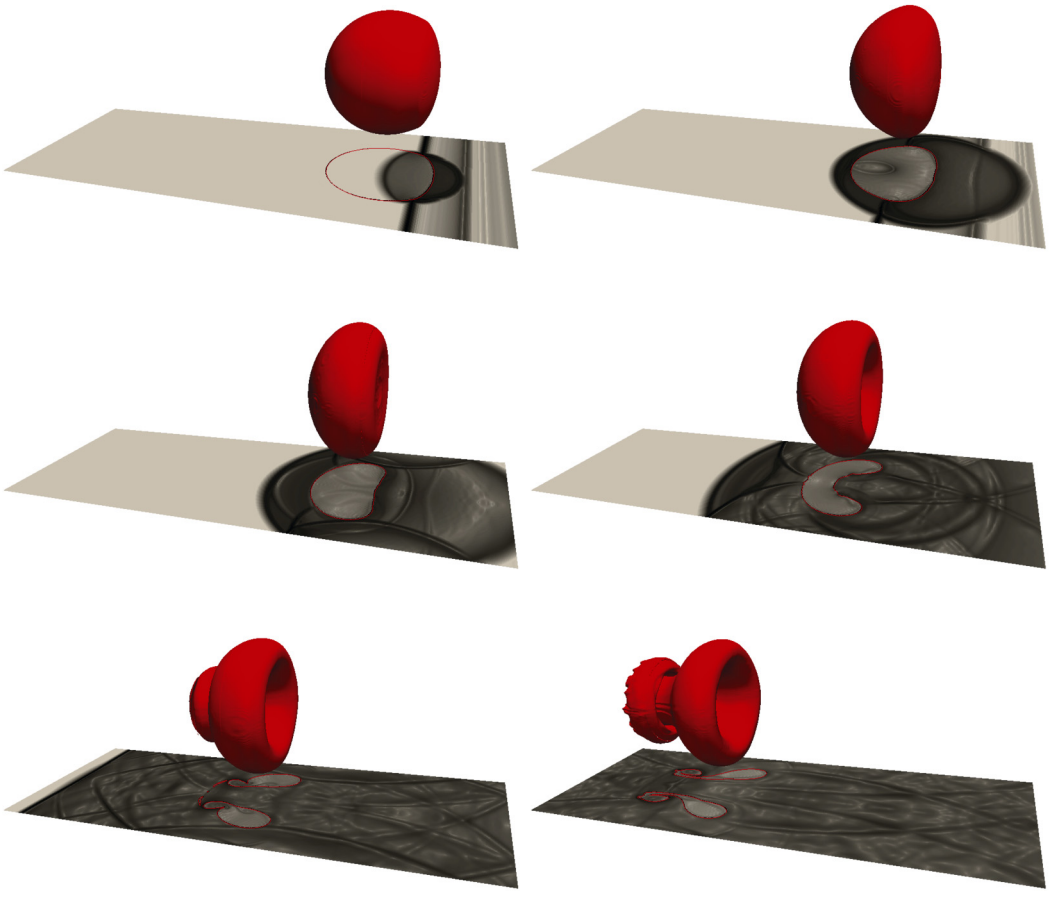


Fig. 6. Interaction of a Mach 1.22 shock propagating in air through an helium bubble (TC1). Pictures at $t = 62$ µs, 110 µs, 163 µs, 264 µs, 471 µs, 735 µs. From left to right, top to bottom.

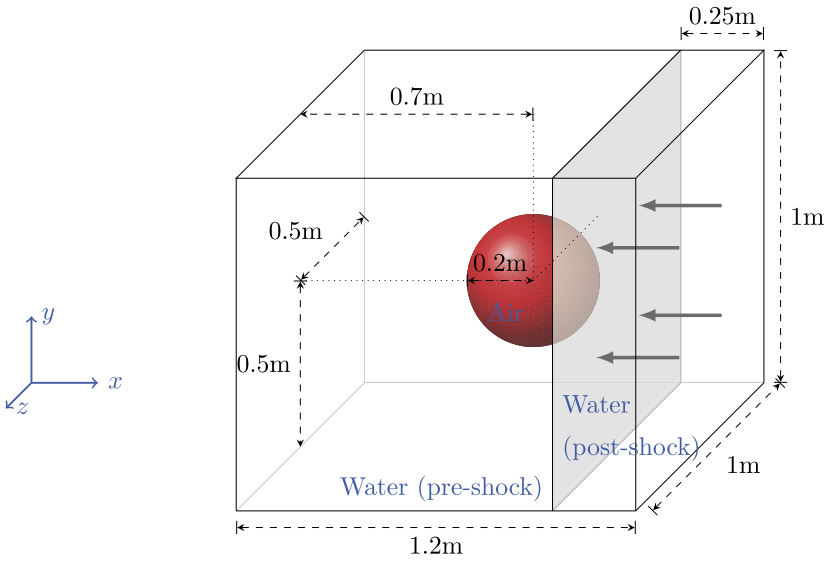


Fig. 7. Sketch of the initial configuration for shock-bubble interaction TC2. The computational domain is $[-0.2, 1] \times [0, 1] \times [0, 1]$ m^3.

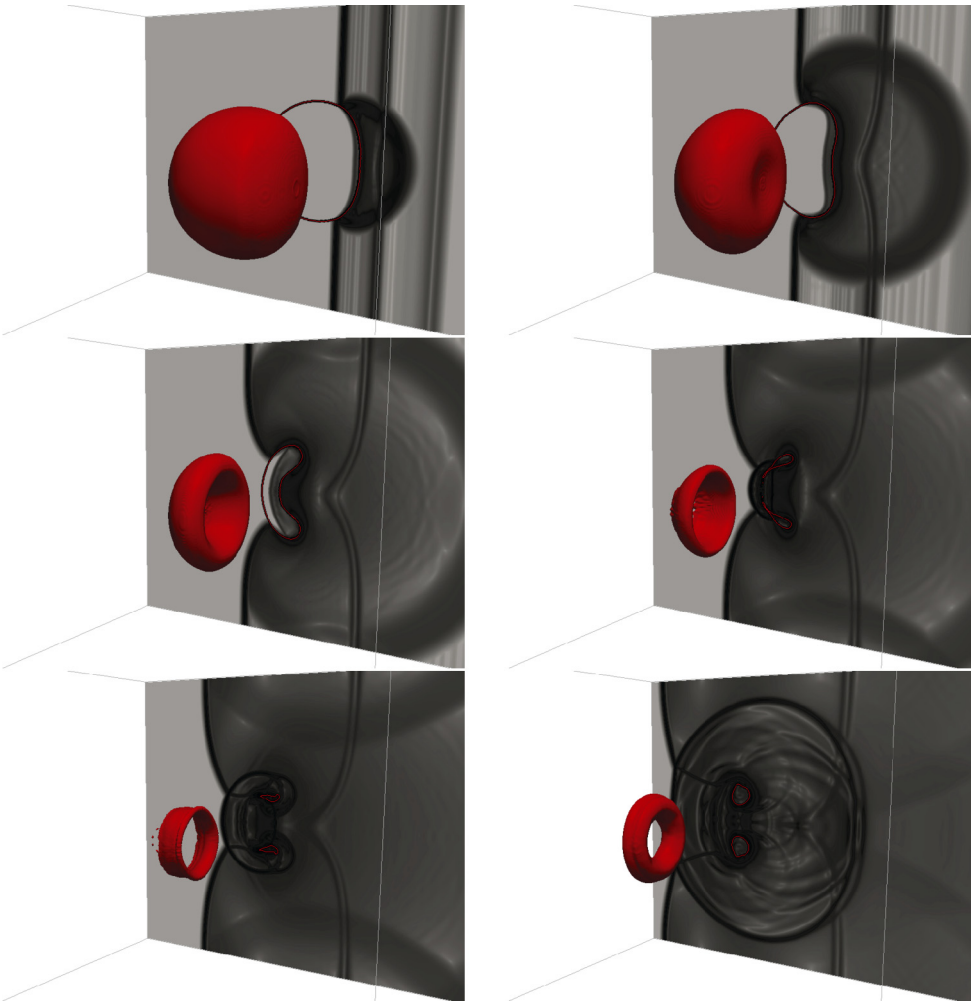


Fig. 8. Interaction of a Mach 1.422 water shock and an air bubble (TC2). Interface and schlieren on the plane $z = 0.5$ at time $t = 37$ µs, 73 µs, 110 µs, 132 µs, 147 µs, 195 µs. From left to right, top to bottom.

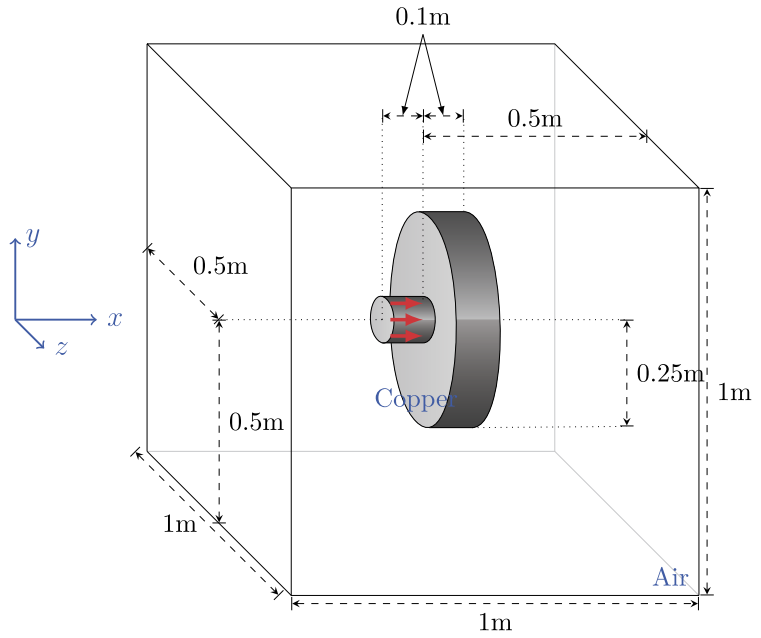


Fig. 9. Sketch of the 3D initial configuration for the impact test case TC3 where a projectile impinges on a cylindrical plate with a velocity of 800 $\mathrm{m\,s^{-1}}$. The computational domain is $[-0.5, 0.5]^3$ $\mathrm{m^3}$.

6.1. Shock–bubble interaction

We consider two shock-bubble interaction test cases involving different fluids. The boundary conditions are fixed at the initial values for inlet and homogeneous Neumann conditions are imposed at outlet. Reflection conditions are imposed for all the other boundaries.

Air–helium shock–bubble interaction

TC1 is the propagation in air of a Mach 1.22 shock through an helium bubble. The initial configuration and the physical parameters are described in Fig. 5 and in Table 1. The computation is performed on a $1000 \times 400 \times 400$ mesh and lasts for 50 h on 300 processors. The zero iso-value of the level set function and schlieren on the horizontal plane through the center of the bubble are presented at different times on Fig. 6.

The results are qualitatively similar to those presented in the literature in two dimensions, see for example [28,12,22,16].

Air–water shock–bubble interaction

TC2 involves a van der Waals gas bubble and a Mach 1.422 shock in water modeled by a stiffened gas constitutive law. The initial configuration and the physical parameters are described in Fig. 7 and in Table 1. This test case is more severe compared to the previous one since it presents larger density ratios. The mesh is $480 \times 400 \times 400$ and the computation lasts 15 h on 96 processors. The results are presented in Fig. 8, where we show the zero of the level set function and the schlieren on the vertical plane through the center of the bubble.

The bubble is strongly compressed, it changes topology and swirls similarly to what happens in two dimensions, see [1,16].

6.2. Impact

We present an impact simulation of a 800 $\mathrm{m\,s^{-1}}$ projectile on a plate in air (TC3). The initial configuration and the physical parameters are described in Fig. 9 and in Table 1. In this simulation the projectile and the plate are adjacent at initial time. The projectile and the plate are a single material and they are described by the same level set. In other words they will necessarily stick together for the whole simulation. Homogeneous Neumann conditions are imposed at the borders. The computation is performed on a 600^3 mesh and uses 216 processors for 60 h.

The results are shown on Fig. 10. The elastic material is deformed and oscillates while being displaced rightward. Schlieren images on the planes $x = 0.03$, $y = 0$ and $z = 0$ are presented. Compared to the two dimensional test case [16] the deformation is less evident as the mass ratio between the projectile and the plate is smaller.

For this test case we present in Table 2 the convergence of the mass and energy conservation errors as functions of the grid refinement. The errors are computed by relative L^1 norms in space and time. The simulations last until the fluxes are zero across the domain boundaries for a mesh of 100^3. This time represents 25% of the total computational time (fourth

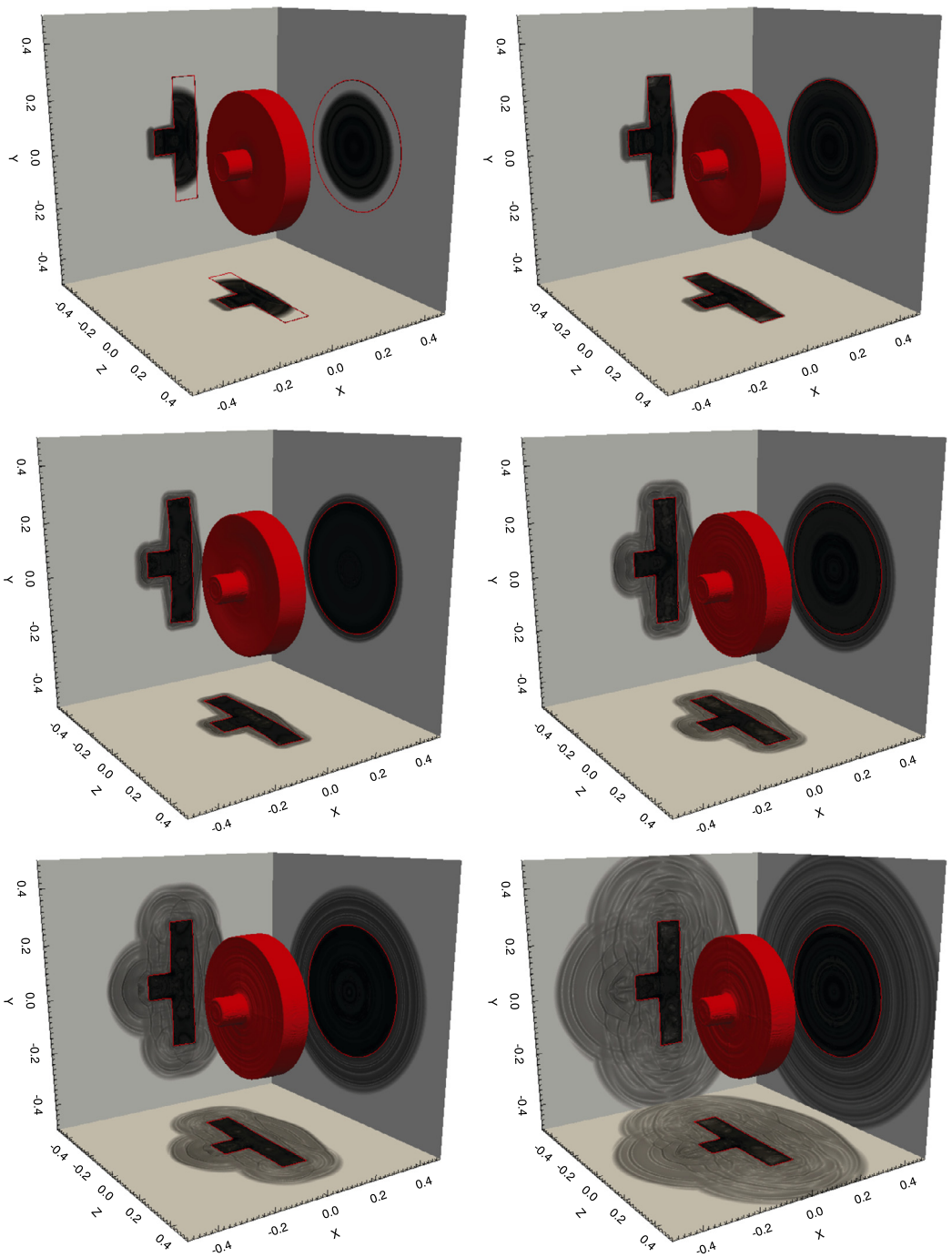


Fig. 10. Impact of a projectile on a plate (TC3). Interface and schlieren at $t = 24$ µs, 43 µs, 88 µs, 178 µs, 355 µs, 710 µs. From left to right, top to bottom.

Table 2
Mass and energy conservation L^1 errors in space and time in percentage of the total mass and energy, respectively, for mesh sizes of 100^3, 200^3 and 400^3 (TC3).

L^1 error	100^3	200^3	400^3
Mass conservation (%)	0.6117	0.2602	0.1145
Energy conservation (%)	0.6155	0.2596	0.1137

Table 3
L^1-norm error in space and time of $|\rho - \rho_0 \det(\nabla_x Y)|$ in percentage of ρ and L^1-Frobenius norm in space and time of $\nabla_x \times (\nabla_x Y)$ for mesh sizes of 100^3, 200^3 and 400^3 (TC3).

L^1 error	100^3	200^3	400^3
$\lvert\rho - \rho_0 \det(\nabla_x Y)\rvert$ (%)	0.2300	0.1456	0.0511
$\lVert\nabla_x \times \nabla_x Y\rVert$	0.1716	0.1258	0.0768

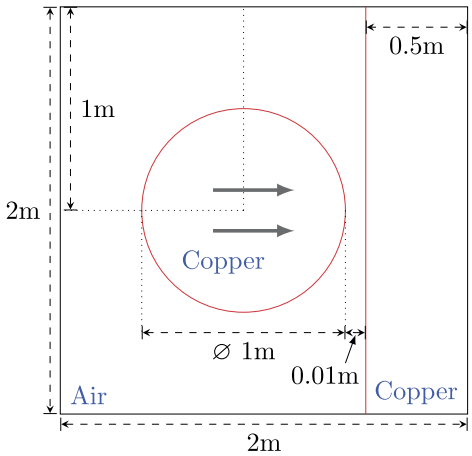


Fig. 11. Sketch of the 2D initial configuration for impact and rebound test case TC4 where a copper disk impinges on a copper layer at velocity 500 m s^{-1}. The computational domain is $[-1, 1]^2$ m^2.

snapshot in Fig. 10). It can be observed that the conservation errors coherently decrease as the mesh is refined with a rate close to 1, as expected. However, for large elongations of the material, like in the case of rubbers, conservation errors may occur due to the level set discretization. For long filaments, it may occur that when a structure is smaller than a computational cell, the isoline zero of the level set function disappears, and with it, the material contained.

Also, we show in Table 3 the relative error between ρ and $\rho_0 \det(\nabla_x Y)$, and the Frobenius norm of $\nabla_x \times \nabla_x Y$ for several mesh sizes. For these computations, we only consider solid cells situated at a distance of 0.025 m from the interface in order to avoid the singularity of the inverse deformation tensor at the border of the elastic solids. The simulations last about half the total computational time (fifth snapshot in Fig. 10). It can be seen that the errors decrease as the mesh is refined, at a rate that is of about 1 for the density, and slightly smaller for $\nabla_x \times \nabla_x Y$, as expected because of the additional differentiation.

6.3. Rebounds

We now focus on cases similar to impacts except that the projectile is not initially adjacent to the plate and can rebound. Here we do not consider the modeling of the full relevant physics at the scales induced by the arbitrarily small gap between the objects getting in contact. However, in terms of numerical modeling this case may need special care in the solution of the Riemann problem when the projectile and the plate get in material contact. Material contact is defined as a configuration where the level sets pertaining to the projectile and the plate are separated by less than a grid point. We model this phenomenon as a frictionless contact where both the normal and the tangential stresses vanish. This allows a discontinuity in both normal and tangential velocities in the solution of the Riemann problem, see equations (53), (54) and (55).

Two-dimensional rebounds

First (TC4), we simulate the solution in two dimensions as the meshes that can be afforded are significantly finer. As depicted on Fig. 11, the first test case is relative to a copper disk moving toward a copper layer on the east boundary. The surrounding fluid is air. The east border of the computational domain acts as a rigid wall where the displacement vanishes in the normal direction. The other borders are modeled by homogeneous Neumann conditions.

The gap between the disk and the plate measures 10^{-2} m and the disk travels at a speed of 500 m s^{-1}. A few snapshots of the solution are presented on Fig. 12. The computations are run on 2000^2 and 4000^2 meshes. The computations last 10 h and 12 h on 144 and 324 processors, respectively.

In the case where the mesh is 2000^2, the rebound takes place thanks to a material contact of the disk with the copper layer. An high speed shock and the corresponding jet emerge from the impact. When the mesh size increases to 4000^2 cells, no contact occurs at the rebound and a thin layer of air cells still separates the two materials. The flow and deformation features observed for a 2000^2 mesh are overall retrieved for a 4000^2 mesh.

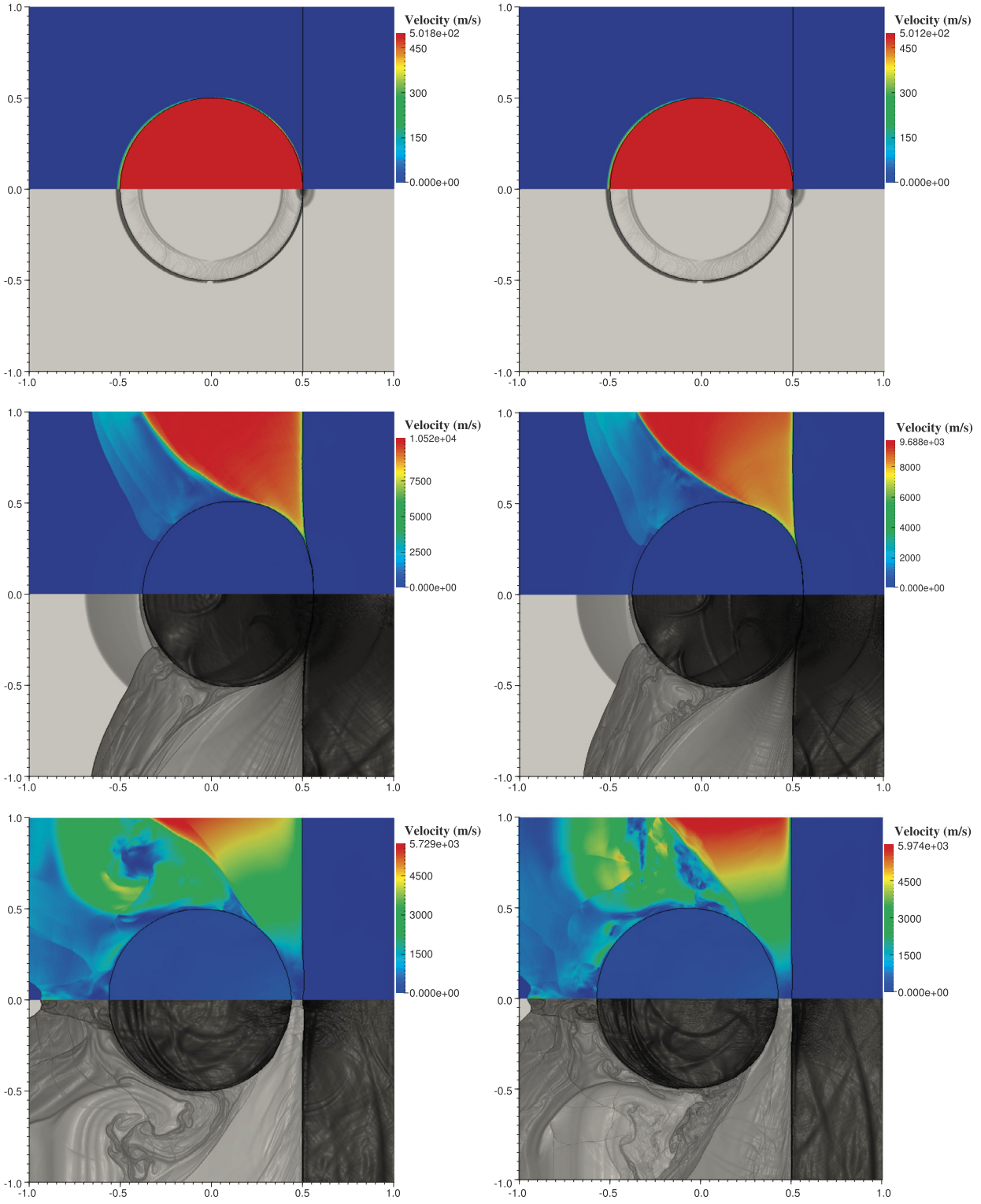


Fig. 12. Impact and rebound of a projectile on a layer in two dimensions (TC4). Velocity and schlieren at time $t = 21$ µs, $t = 450$ µs and $t = 900$ µs from top to bottom. The mesh is 2000^2 on the left and 4000^2 on the right.

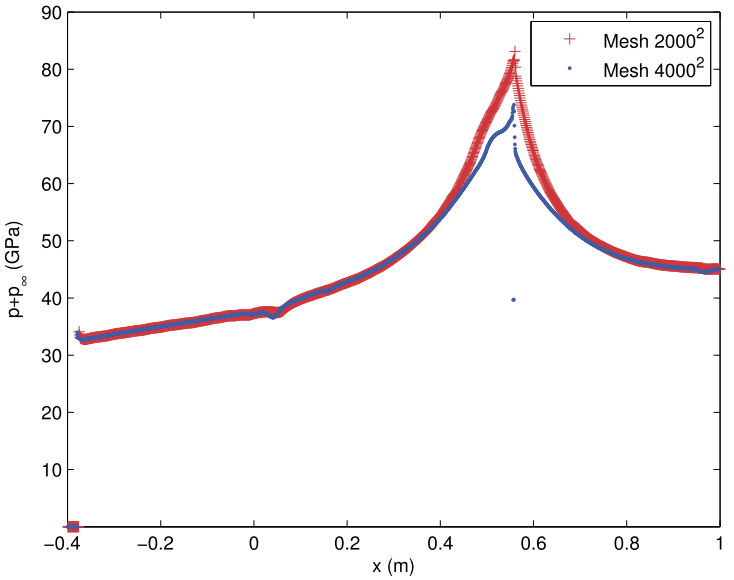


Fig. 13. Pressure on the line $y = 0$ in the range $x \in [-0.4, 1]$ at time $t = 450$ µs.

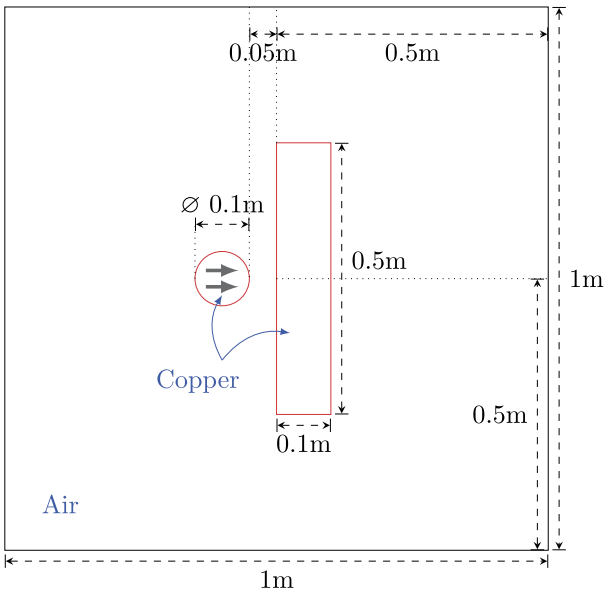


Fig. 14. Sketch of the 2D initial configuration for impact and rebound test case TC5 where a projectile impinges a plate at velocity 800 $\mathrm{m\,s^{-1}}$. The computational domain is $[-0.5, 0.5]^2$ $\mathrm{m^2}$.

The pressure through $y = 0$ for both meshes is presented on Fig. 13. We can observe a significant pressure peak at the contact interface compressing the material and therefore the surrounding fluid that is ejected from the contact region at high speed.

TC5 is relative to the impact of a the projectile at 800 $\mathrm{m\,s^{-1}}$ initially detached from a shield in two dimensions. The initial configuration and the physical parameters of the two-dimensional simulation are described in Fig. 14 and in Table 1. The computation is performed on a 4000^2 mesh and uses 24^2 processors for 6 h.

Here the disk actually rebounds on an shock layer created in front of the disk. This layer has a thickness of a few grid points. Again a high speed shock forms at the impact. The speed of this shock is of the order of that of the fast waves in the elastic solid. These results show that the overall scheme is robust on very fine meshes for stiff numerical simulations (see Fig. 15).

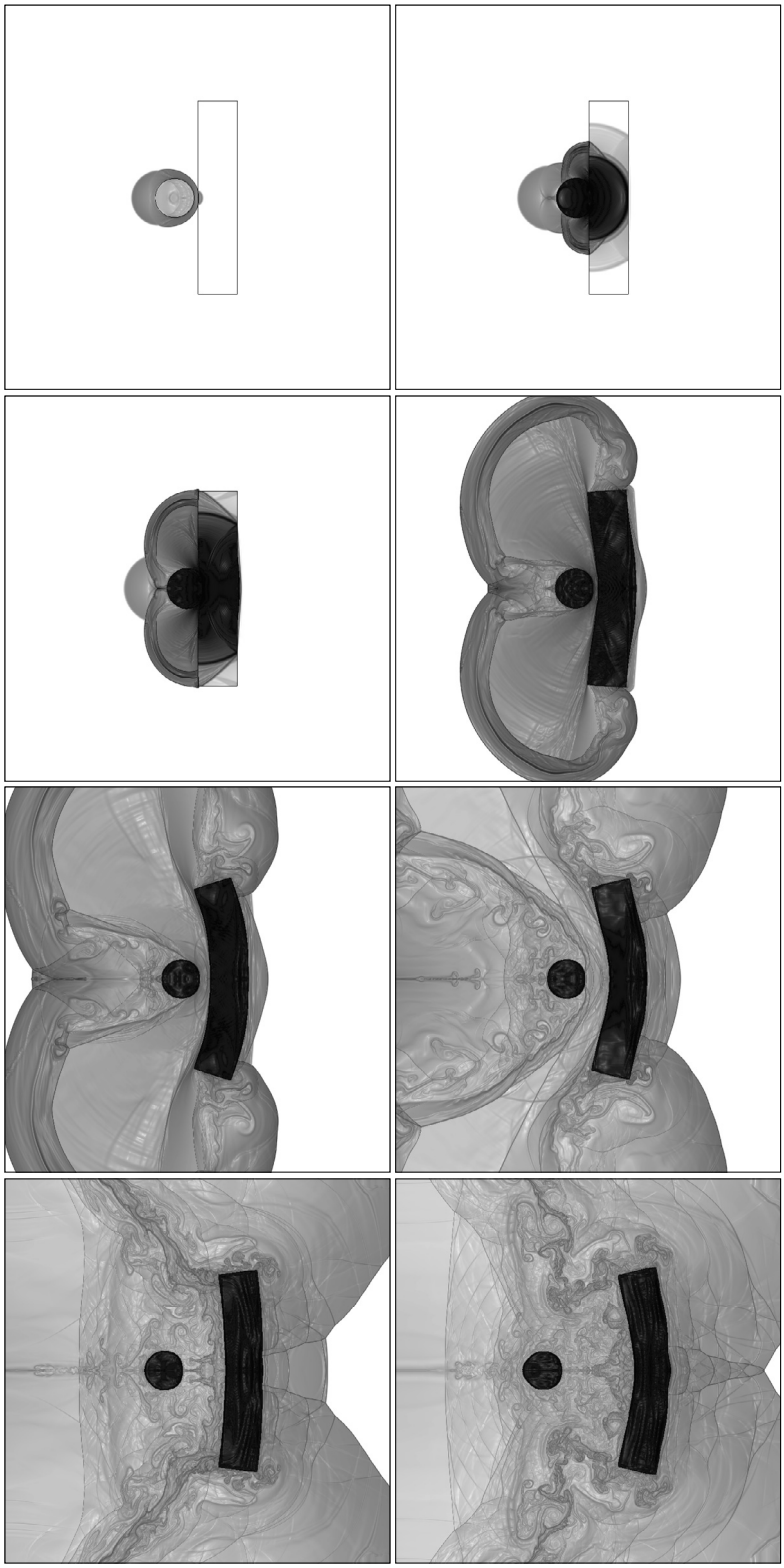


Fig. 15. Impact and rebound of a projectile on a plate in two dimensions (TC5). Interface and schlieren at $t = 50$ µs, 83 µs, 99 µs, 149 µs, 199 µs, 298 µs, 497 µs, 710 µs. From left to right, top to bottom.

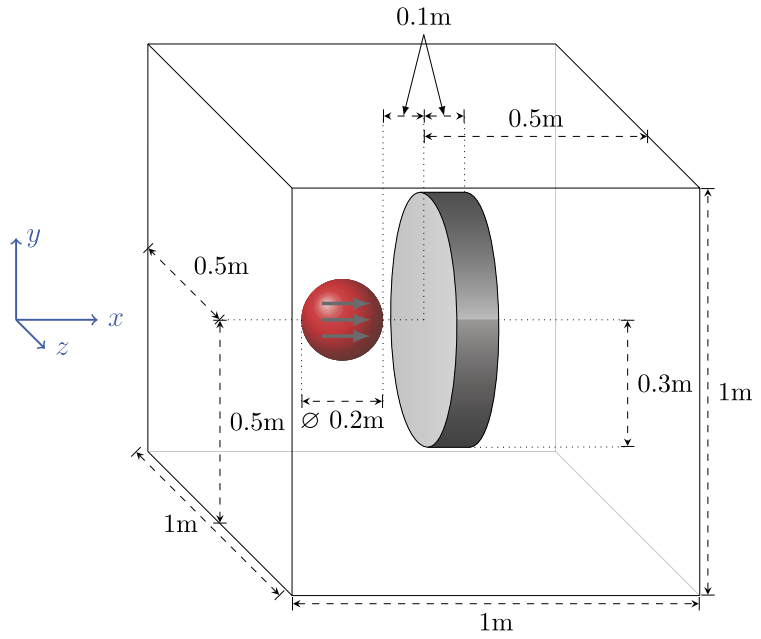


Fig. 16. Sketch of the initial configuration for the impact test case TC6 where a projectile impinges a shield at velocity 800 $\mathrm{m\,s^{-1}}$ and rebounds. The computational domain is $[-0.5, 0.5]^3$ $\mathrm{m^3}$.

Three-dimensional rebound

The initial configuration and the physical parameters of the three-dimensional rebound (TC6) are described in Fig. 16 and in Table 1. The computation is performed on a 400^3 mesh and uses 216 processors for 24 hours.

Overall the physics of the interaction is similar to what observed in two dimensions. In the figure the level set of the shield is in blue, whereas as the sphere is red. The level sets are also projected on the visualized planes (see Fig. 17).

7. Conclusions and future work

We have presented a three-dimensional multimaterial model that describes the dynamics of the interaction between gas, liquids and neohookean materials. This model is hyperbolic and reduces to the well known linear model in the small-deformation limit. The numerical scheme is based on an approximate Riemann solver that is able to model multimaterial interfaces with possibly frictionless contacts. The scheme is simple to implement, stable and robust, as shown by the stiff test cases presented.

The explicit solver proposed is constrained by the time scale of the elastic waves. For problems such as impacts or in general fast-dynamical processes, this is the relevant scale of the physical phenomenon. For physical phenomena that take place on the time scale determined by the material velocity, the stability condition limits the application of such time-dependent approaches. Also, the significantly different time scales present in multimaterial phenomena introduce accuracy and efficiency problems that are well known in low-speed compressible fluids. Future work will include exploration of these issues for compressible multimaterial flows, as well as, enriching the model with plasticity.

Acknowledgements

This study has been carried out with financial support from the French State, managed by the French National Research Agency (ANR) in the frame of the 'Investments for the future' Programme IdEx Bordeaux-CPU (ANR-10-IDEX-03-02). The simulations presented in this paper were carried out using the PLAFRIM experimental parallel testbed, being developed under the Inria PlaFRIM development action with support from LABRI and IMB and other entities: Conseil Régional d'Aquitaine, FeDER, Université de Bordeaux and CNRS (see https://plafrim.bordeaux.inria.fr/). Alexia De Brauer is supported by a grant from the DGA (Délégation Générale de l'Armement, Ministère de la Défense).

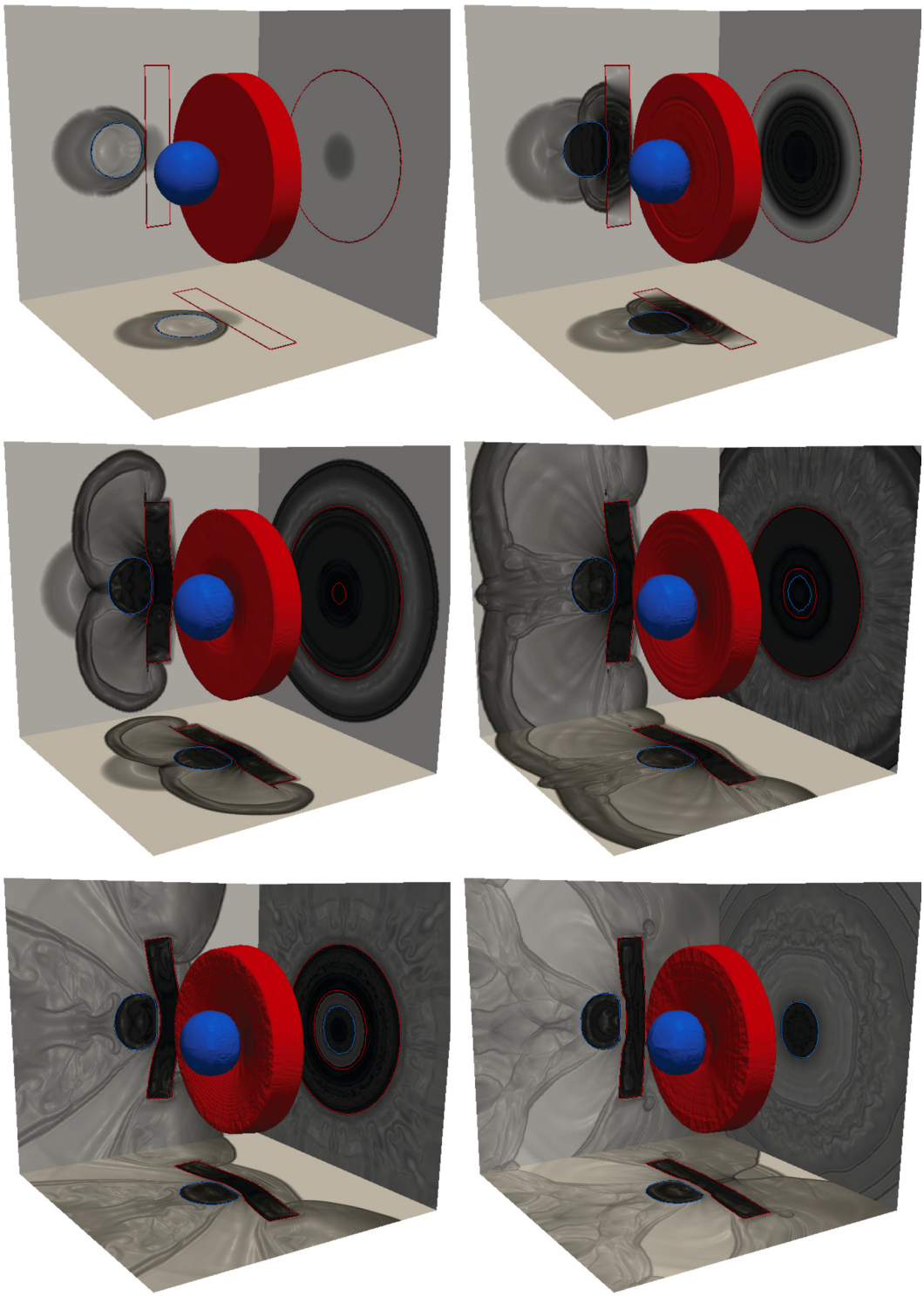


Fig. 17. Impact of a projectile on a shield (TC6). Interface and schlieren on the planes $x = 0.025$ and $y = z = 0$ at $t = 107$ µs, 166 µs, 206 µs, 256 µs, 383 µs, 710 µs. From left to right, top to bottom. (For interpretation of the references to color in this figure, the reader is referred to the web version of this article.)

References

[1] G. Allaire, S. Clerc, S. Kokh, A five-equation model for the simulation of interfaces between compressible fluids, J. Comput. Phys. 181 (2) (2002) 577–616.
[2] P.T. Barton, R. Deiterding, D. Meiron, D. Pullin, Eulerian adaptive finite-difference method for high-velocity impact and penetration problems, J. Comput. Phys. 240 (C) (2013) 76–99.
[3] P.T. Barton, D. Drikakis, An Eulerian method for multi-component problems in non-linear elasticity with sliding interfaces, J. Comput. Phys. 229 (15) (2010) 5518–5540.
[4] P.T. Barton, D. Drikakis, E. Romenski, V.A. Titarev, Exact and approximate solutions of Riemann problems in non-linear elasticity, J. Comput. Phys. 228 (18) (2009) 7046–7068.
[5] P.T. Barton, B. Obadia, D. Drikakis, A conservative level-set based method for compressible solid/fluid problems on fixed grids, J. Comput. Phys. 230 (21) (2011) 7867–7890.
[6] M. Berndt, J. Breil, S. Galera, M. Kucharik, P.-H. Maire, M. Shashkov, Two-step hybrid conservative remapping for multimaterial arbitrary Lagrangian–Eulerian methods, J. Comput. Phys. 230 (17) (2011) 6664–6687.
[7] G.H. Cottet, E. Maitre, T. Milcent, Eulerian formulation and level set models for incompressible fluid–structure interaction, ESAIM: Math. Model. Numer. Anal. 42 (2008) 471–492.
[8] S. Davis, Simplified second-order Godunov-type methods, SIAM J. Sci. Stat. Comput. 9 (3) (1988) 445–473.
[9] N. Favrie, S. Gavrilyuk, S. Ndanou, A thermodynamically compatible splitting procedure in hyperelasticity, J. Comput. Phys. 270 (C) (2014) 300–324.
[10] N. Favrie, S.L. Gavrilyuk, Diffuse interface model for compressible fluid – compressible elastic–plastic solid interaction, J. Comput. Phys. 231 (7) (2012) 2695–2723.
[11] N. Favrie, S.L. Gavrilyuk, R. Saurel, Solid–fluid diffuse interface model in cases of extreme deformations, J. Comput. Phys. 228 (16) (2009) 6037–6077.
[12] R.P. Fedkiw, T. Aslam, B. Merriman, S. Osher, A non-oscillatory Eulerian approach to interfaces in multimaterial flows (the ghost fluid method), J. Comput. Phys. 152 (1999) 457–492.
[13] S. Galera, P.-H. Maire, J. Breil, A two-dimensional unstructured cell-centered multi-material ALE scheme using VOF interface reconstruction, J. Comput. Phys. 229 (16) (2010) 5755–5787.
[14] S.L. Gavrilyuk, N. Favrie, R. Saurel, Modelling wave dynamics of compressible elastic materials, J. Comput. Phys. 227 (5) (2008) 2941–2969.
[15] S.K. Godunov, Elements of Continuum Mechanics, Nauka, Moscow, 1978.
[16] Y. Gorsse, A. Iollo, T. Milcent, H. Telib, A simple cartesian scheme for compressible multimaterials, J. Comput. Phys. 272 (2014) 772–798.
[17] D.J. Hill, D. Pullin, M. Ortiz, D. Meiron, An Eulerian hybrid WENO centered-difference solver for elastic–plastic solids, J. Comput. Phys. 229 (24) (2010) 9053–9072.
[18] G.A. Holzapfel, Nonlinear Solid Mechanics. A Continuum Approach for Engineering, J. Wiley and Sons, 2000.
[19] G.S. Jiang, C.W. Shu, Efficient implementation of weighted ENO schemes, J. Comput. Phys. 126 (1) (1996) 202–228.
[20] G. Kluth, B. Despres, Discretization of hyperelasticity on unstructured mesh with a cell-centered Lagrangian scheme, J. Comput. Phys. 229 (24) (2010) 9092–9118.
[21] P.-H. Maire, R. Abgrall, J. Breil, R. Loubère, B. Rebourcet, A nominally second-order cell-centered Lagrangian scheme for simulating elastic–plastic flows on two-dimensional unstructured grids, J. Comput. Phys. 235 (C) (2013) 626–665.
[22] A. Marquina, P. Mulet, A flux-split algorithm applied to conservative models for multicomponent compressible flows, J. Comput. Phys. 185 (1) (2003) 120–138.
[23] G.H. Miller, An iterative Riemann solver for systems of hyperbolic conservation laws, with application to hyperelastic solid mechanics, J. Comput. Phys. 193 (1) (2003) 198–225.
[24] G.H. Miller, P. Colella, A conservative three-dimensional Eulerian method for coupled solid–fluid shock capturing, J. Comput. Phys. 183 (1) (2002) 26–82.
[25] S. Ndanou, N. Favrie, S. Gavrilyuk, Criterion of hyperbolicity in hyperelasticity in the case of the stored energy in separable form, J. Elast. 115 (1) (2013) 1–25.
[26] B.J. Plohr, D.H. Sharp, A conservative Eulerian formulation of the equations for elastic flow, Adv. Appl. Math. 9 (1988) 481–499.
[27] B.J. Plohr, D.H. Sharp, A conservative formulation for plasticity, Adv. Appl. Math. 13 (1992) 462–493.
[28] J. Quirk, S. Karni, On the dynamics of a shock–bubble interaction, J. Fluid Mech. 318 (1) (1996) 129–163.
[29] E.F. Toro, M. Spruce, W. Speares, Restoration of the contact surface in the HLL-Riemann solver, Shock Waves 4 (1994) 25–34.